ANL/ES-C1200101

Particulate Emissions Control using Advanced Filter Systems

Final Report for Argonne National Laboratory, Corning Inc. and Hyundai Motor Company CRADA Project

Energy Systems Division

ANL/ES-C1200101

Particulate Emissions Control using Advanced Filter Systems

Final Report for Argonne National Laboratory, Corning Inc. and Hyundai Motor Company CRADA Project

prepared by
Hee Je Seong and Seungmok Choi
Energy Systems Division, Argonne National Laboratory

October 9, 2015

Objective:

This is a 3-way CRADA project working together with Corning, Inc. and Hyundai Motor Co. (HMC). The project is to understand particulate emissions from gasoline direct-injection engines (GDI) and their physico-chemical properties. In addition, this project focuses on providing fundamental information about filtration and regeneration mechanisms occurring in gasoline particulate filter (GPF) systems. For the work, Corning provides most advanced filter substrates for GPF applications and HMC provides three-way catalyst (TWC) coating services of these filter by way of a catalyst coating company. Then, Argonne National Laboratory characterizes fundamental behaviors of filtration and regeneration processes as well as evaluated TWC functionality for the coated filters. To examine aging impacts on TWC and GPF performance, the research team evaluates gaseous and particulate emissions as well as back-pressure increase with ash loading by using an engine-oil injection system to accelerate ash loading in TWC-coated GPFs.

1. Introduction

GDI engines have gradually increased the popularity as a propulsion system for light-duty passenger vehicles and this trend is expected to continue. As upcoming emissions regulations require significant reductions in PM emissions from GDI engines, there have been on-going research on how to meet the regulations by way of fuel injection strategies and emissions control systems. Diesel particulates have been well characterized, so their characterization helped better understand soot formation and oxidation processes in engine cylinder. While diesel and GDI engines are similarly configured in the sense that fuel is directly injected into engine cylinders, GDI particulates produced through homogeneous combustion need more investigations to understand soot formation and oxidation processes. For instance, GDI engines emit particles in a wide size range [1], contributing to a large number of particles, despite low mass concentration. There are many reports on particle number and mass emissions from GDI engines, whereas there are few on detailed properties of GDI particulates.

GPFs are considered an enabling technology to meet stringent particulate regulations. However, fuel economy penalties resulting from increased back-pressure and system cost increase partially offset benefits of fuel savings from direct injection. Since TWC converters effectively reduce CO, HC and NOx from spark ignition (SI) engines, the TWC-coated GPF (TWC/GPF) concept is a logical development for GDI engines. While TWC and TWC/GPF were initially configured as separate blocks, one single block of TWC/GPF is considered the ideal configuration because of the space savings and potential cost reduction. However, long-term TWC functionality as well as GPF performance with ash loading are not much known. Accordingly, filter substrates are developed for GPF applications available at single or separate blocks, in consideration of low back-pressure increase with TWC coating and ash loading at high exhaust temperatures. It is typically known that soot loading in GPF is not a concern because soot mass emissions are low and loaded soot in the filter is easily oxidized at high exhaust temperatures. However, detailed regeneration mechanism is not well examined.

In this CRADA project, therefore, the research team evaluated various aspects of GDI particulates and GPF research by leveraging unique capabilities among three partners. There

have been fundamental examinations of GDI particulate emissions, their physico-chemical properties and oxidative reactivity. In the separate tasks, GPF filtration and regeneration processes were further investigated in a visualization set-up and bench-scale flow reactor mounted in a GDI engine at actual operation conditions.

2. Experimental

2.1 Installation of HMC theta-II GDI engine and GPF bench test system

A theta-II GDI engine from HMC was mounted on a 112 kW blower-cooled AC dynamometer for speed control and torque measurements (Figure 2.1a). The engine geometry and specifications are given in Table 2.1. In consideration of engine cell configuration, the TWC converter and muffler were lined on the floor. Two pieces of wall-through type TWC were installed at about 4 ft downstream of exhaust manifold to convert regulatory gaseous emissions, CO, HC, and NOx. An open electric control unit (ECU) received from HMC controls fuel injection parameters, so that gaseous and particulate emissions can be examined at various conditions. ETAS hardware and INCA software interfaces were used to access the engine electronic control unit (ECU) to adjust the injection timing. The engine exhaust emissions were measured by using an exhaust gas analyzer (Horiba MEXA 7100-DEGR) (Figure 2.1b), and soot mass concentration was measured using a high-sensitivity photo-acoustic sensor (AVL 483 micro soot sensor) (Figure 2.1c). Particle sizes were measured by using a scanning mobility particle sizer (SMPS) (TSI, model 3936) coupled with Dekati dilution system. In this work, the certified Tier 2 EEE gasoline fuel and commercially available ILSAC GF-5 motor oil that was API SN rated with an SAE grade of 5W-20 were used.

A bench-scale GPF system was installed to examine filtration efficiency, pressure drop and regeneration process. In consideration of add-on type, a portion of exhaust gas leading to the GPF was bypassed from the downstream of the TWC. The GPF used a bisected GPF (half cut of 2” (D) x 6” (L)) and the top side was covered with quartz glass for clear observations of filtration and regeneration processes, which were monitored using a CCD camera and stereo microscope as shown in Figure 2.2. The gas flow from the engine is described in Figure 2.3.

(a) (b) (c)

Figure 2.1 (a) Hyundai GDI engine, (b) Horiba emissions bench, and (c) AVL micro soot sensor.

Table 2.1 GDI engine geometry and specifications.

Compression ratio	11.3
Bore (mm)	88
Stroke (mm)	97
Displacement (cm^3)	2,359
Number of cylinders	4
Rated power (kW)	147.8 @ 6,300 rpm
Rated torque (Nm)	250 @ 4,250 rpm

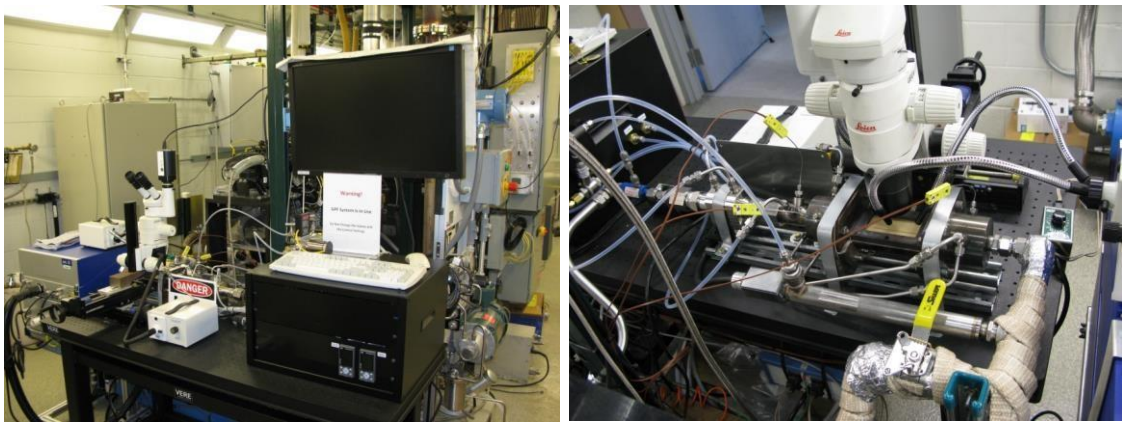

(a) (b)

Figure 2.2 (a) GPF reactor and visualization system, and (b) bench-scale optical set-up.

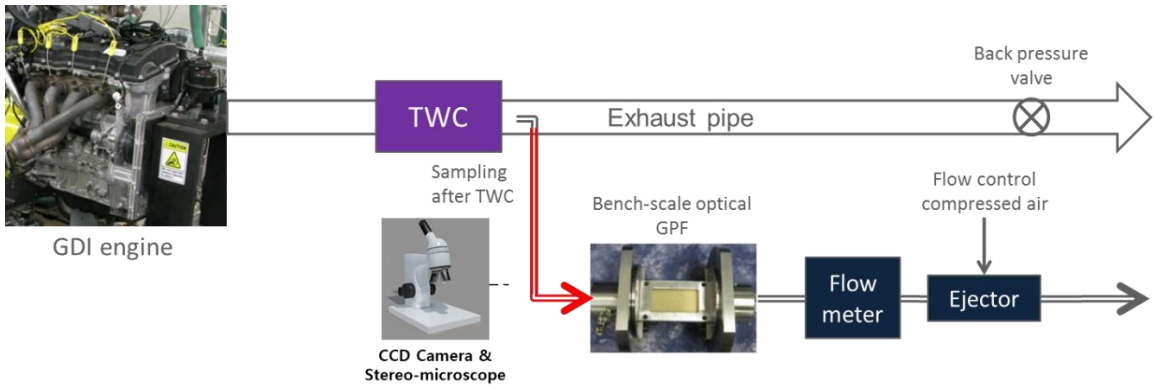

Figure 2.3 Schematic of exhaust gas stream to the GPF reactor.

Since the visualization set-up had several issues in controlling exhaust temperatures, monitoring exhaust emissions and leaking, it has been fully replaced by a bench-scale flow reactor as below in Figure 2.4. A short path from the exhaust pipe enables to utilize hot exhaust gases as engine modes change. Also, an air heater is installed right before the flow reactor to oxidize soot remaining in the filter because pressure drop and other parameters need to be analyzed at no soot loading condition for the fair comparison. In addition, an engine-oil injection system, composed of a lube oil tank, oil line, solenoid valve and pulse generator, is

added to have a capability that ages filters in an acceleration mode. The cylindrical filter used in the reactor has a dimension of 2”(D)X6”(L).

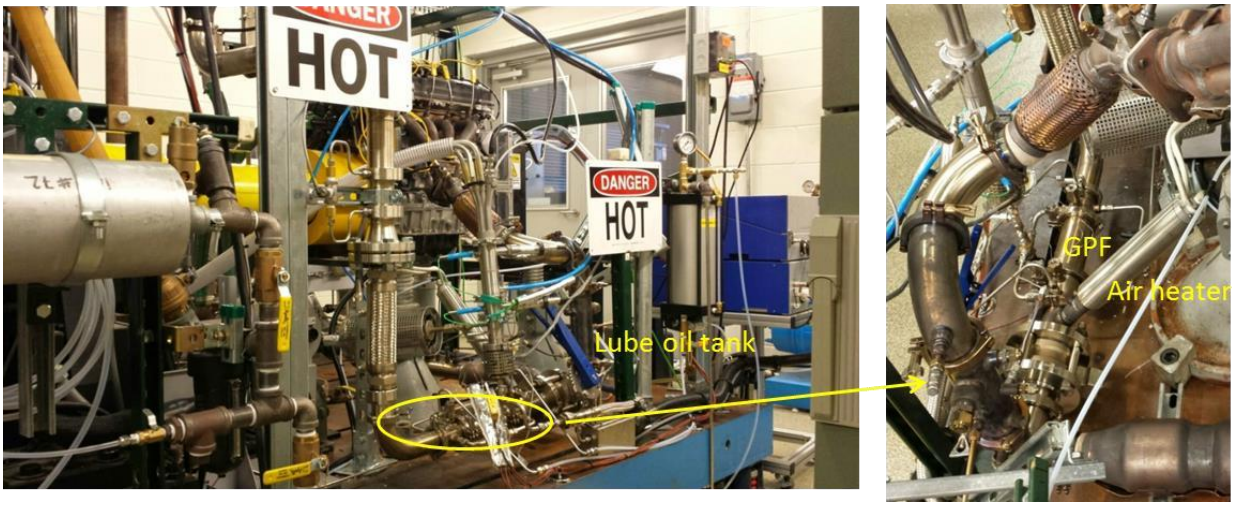

Figure 2.4 Bench-scale flow reactor system installed in the GDI engine.

2.2 GDI PM morphology and soot characterization

To examine GDI PM properties, fundamental research has been performed for GDI particulates sampled at various conditions. For the work, thermophoretic sampling was conducted using an Argonne-developed thermophoretic sampler for transmission electron microscopy (TEM) analysis (Figure 2.5). This analysis does not require dilution and other systems for hydrocarbon removal and sampling time is controlled by adjusting the number of sampling and residence time to have optimized numbers of particles on TEM grids. The principle of the sampling is described as follows. An exhaust stream bypassed from the exhaust pipe was insulated to keep it from being condensed. A sampling tip loaded with a TEM-grid is inserted like a frog tongue into a sampling chamber connected to the bypassed exhaust stream by using a pneumatic actuator with electric signal of a time resolution of 20 ms. Since there is a temperature difference between outside TEM-grid and particles in hot exhaust gas, particles migrate onto the TEM grid by thermophoretic effects. The TEM-grid loaded with particles are to be analyzed in a TEM instrument for detailed morphology and nanostructures. (a)

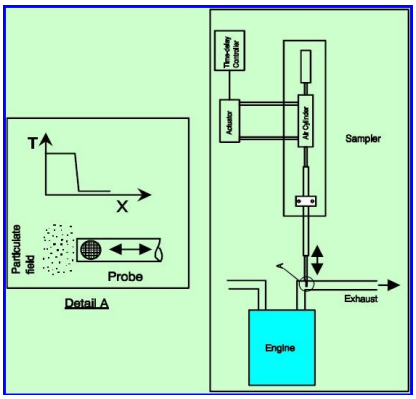

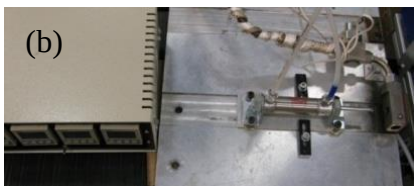

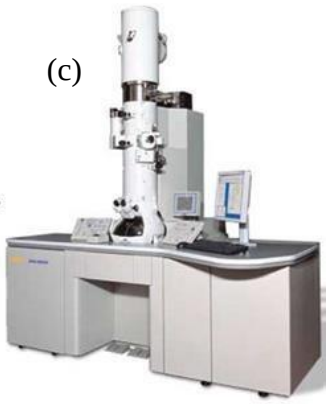

Figure 2.5 (a) Schematic of thermophoretic sampler system, (b) thermophoretic sampler, (c) TEM instrument

The thermophoretic sampling was performed in the upstream of TWC as shown in Figure 2.6 and the engine operating conditions are indicated in Table 2.2. Since there was a difficulty in conducting thermophoretic sampling in the downstream of TWC due to pressure decrease, TWC impacts on particle numbers and mass were examined using a micro soot sensor and SMPS as explained in the later page.

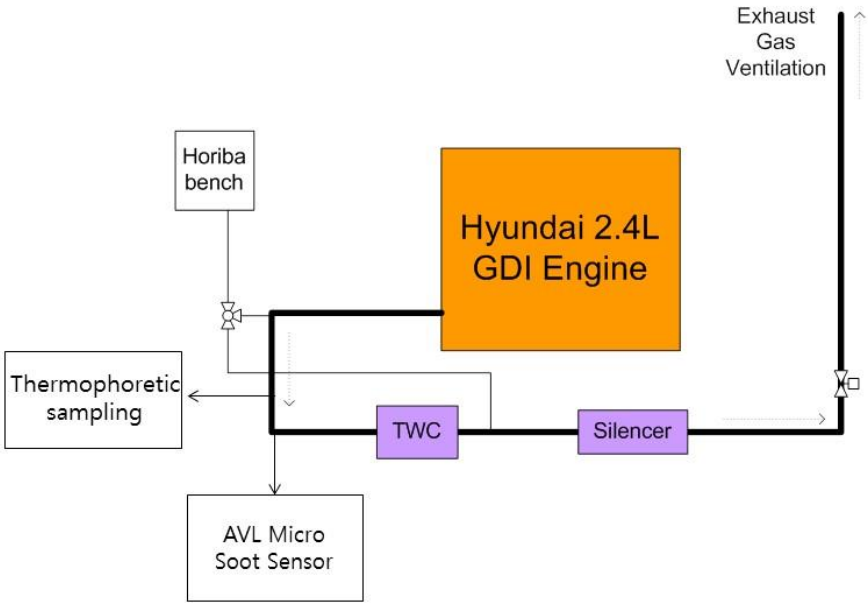

Figure 2.6 Schematic of the engine and sampling system. Table 2.2 Engine operating conditions.

Speed-Load Sweep	
Speed	Load
1,500 rpm **3,000 rpm**	25, 50, 75%
Injection Timing Sweep	
Speed-Load	Injection Timing (˚ bTDC)
1,500 rpm – 50%	330, 300, 260, 260, 230, 190 (spark timing was fixed constant at 25 ˚ bTDC)

The morphology of particle aggregates was analyzed based on 150 – 250 primary and aggregate particles for each case. Figure 2.7 shows a schematic of a chain-like aggregate

composed of primary particles. Primary particle sizes (d_p) were measured directly from TEM images and aggregate sizes (R_g) were calculated by using a customized digital image processing/data acquisition system from the following equations.

The radius of gyration of a single aggregate is defined by the following equation:

$$R_g = \sqrt{\frac{1}{n}\sum_{i=1}^{n} r_i^2} \qquad (2.1)$$

where r_i is the distance from the centroid of the associated aggregate to the center of an individual primary particle, and n is the number of primary particles within a single aggregate particle. Although 2-dimensional projected images in TEM cannot show some hidden particles in 3dimenstional space, R_g in 3-dimensional space is assumed to equal to the R_g in 2-D for a binary projection.

The number (n) of primary particles was determined by the following equation: 1.09

$$n = \left(\frac{A_a}{A_p}\right) \qquad (2.2)$$

where A_a is the projected area of an aggregate, A_p is the projected area of a primary particle, and α is 1.09. The number of primary particles is also defined by:

$$n = k_f \left(\frac{R_g}{d_p}\right)^{D_f} \qquad (2.3)$$

where D_f is fractal dimension to represent compactness of chain-like aggregates.

By taking the log of both sides in eqn. (2.3),

$$\log n = D_f \cdot log\left(\frac{R_g}{d_p}\right) + log(k_f) \qquad (2.4)$$

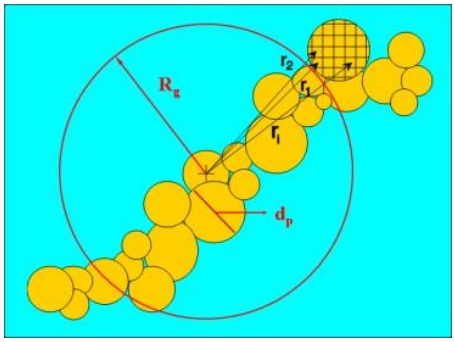

Figure 2.7 Schematic of an aggregate particle composed of several primary particles.

2.3 Characterization of soot properties

The collected particulate samples were observed to analyze the morphology by using a JEOL JEM-2100F. For nanostructures, the samples were examined in detail by using a high-resolution TEM. The TEMs are presently the only instrument that can illuminate the ambiguity of the nanoparticles often found in size measurements by the commercial size-measurement instruments. The TEM micrographs were then digitized by a high-resolution charge-coupled device (CCD) camera and a computer system connected to the TEM. Then the detailed morphological properties of particles, such as sizes and fractal geometry, were analyzed by a custom image processing/data acquisition system (The detailed procedure is referenced in Yazicioglu et al. [2]). Further detailed examinations of the particulate nanostructures were performed at a high-resolution TEM mode, which required sophisticated operating procedures,

such as objective lens corrections. This angstrom-resolution examination can illuminate differences in particle nanostructures among various samples.

Thermogravimetric analysis (TGA) was performed in a Q50 thermogravimetric analyzer from TA Instruments for collected bulk PM samples to evaluate PM oxidative reactivity. Each PM sample was placed in a platinum sample cup and was heated under N_2 gas with a flow rate of 100 ml/min to 600 °C. The sample was pretreated for 60 minutes at 600 °C to drive off volatile compounds, from which VOF was measured. Then, N_2 gas was replaced by air and N_2 mixture (oxygen concentration of 8%) at the same temperature to oxidize the sample. The remaining soot mass was instantaneously measured until soot oxidation was completed. After then, the weight of the unburned residue was measured to evaluate ash content (residue weight/initial PM weight).

Raman spectra of PM samples were obtained on a Renishaw Raman Microscope (In Via). A 50X objective lens of the microscope was used to focus and collect spectra using 633 nm (HeNe laser source) in a Raman shift range of 500 to 2500 cm^{-1}. The spectra were curve-fitted via

IGOR Pro 6.22A software (Wavemetrics Inc.), where 3 Lorentzian-shaped G (~1580 cm^{-1}), D1 (~1360 cm^{-1}) and D4 (~1180 cm^{-1}), and 1 Gaussian-shaped D3 (~1500 cm^{-1}) were obtained with a linear baseline. The area of D3 band (A_{D3}), the ratio of D1 area to G area (A_{D1}/A_G) and D1 full width at half maximum (D1 FWHM) were used as Raman parameters to determine the order of the carbon crystalline structure.

Fourier Transform Infrared (FTIR) spectra were obtained in a wavenumber range of 600 to 4000 cm^{-1}, using a Bruker Vertex 70 spectrometer equipped with a PIKE Technologies MIRacle attenuated total reflectance (ATR). The spectra of each GDI PM sample loaded in a ZeSe crystal were averaged over 32 scans with 1 cm^{-1} resolution.

High resolution synchrotron powder diffraction data were collected using beamline 11-BM at the Advanced Photon Source (APS), Argonne National Laboratory using an average wavelength of 0.414169 Å. Discrete detectors covering a 2θ range from 0.5° to 50° were scanned at room temperature with a step size of 0.001°; therefore this scan covers a *d*-spacing range of 45 Å - 0.5 Å.

The XANES measurements were carried out in beamline 9-BM-C at the APS, Argonne National Laboratory. The samples were pelletized and mounted in a specially designed sample holder where the sample pellet was positioned 45° facing the incident beam, and measurements at the S K-edge were recorded in fluorescence yield mode to observe sulfur oxidation states during soot oxidation. The data was analyzed using the Athena software package.

3. Results

3.1 Characterization of GDI particulates

Figure 3.1 shows TEM images at three selected engine operating conditions as examples. Overall, aggregates were appeared to be chain-like structures as found in particles from other combustions sources. It is interesting to note that there found many small aggregates in the range of sub-50-nm as well as aggregates larger than 200 – 500 nm in length. Such small aggregates were shown to be composed of small nanoparticles.

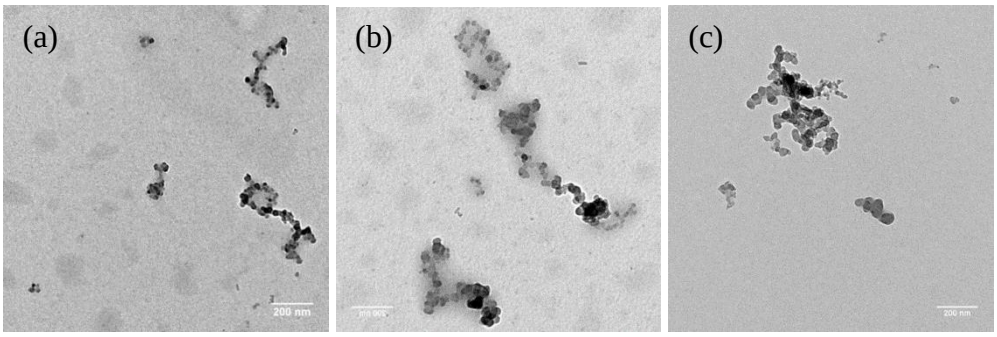

Figure 3.1 TEM images taken at 15kX: (a) 1500rpm-50% load-190° bTDC, (b) 1500rpm-50% load-300° bTDC, and (c) 1500rpm-50% load-330° bTDC.

Highly-magnified TEM images indicated that these sub-50-nm particles are mostly soot particles, characterized by concentric fringe patterns, when they are larger than 20 nm in length as shown in Figure 3.2. Because the background of TEM-grids is amorphous carbon, however, particles with amorphous carbon like young soot are difficult to identify as Figure 3.2c (these particles still remained without evaporation even after high-magnification measurements). Despite difficulties, it is quite convincing that many of GDI nanoparticles in the sub-23-nm range are thought to be solid carbon particles from this analysis. This is a unique finding because such small nanoparticles are rarely observed for diesel engines.

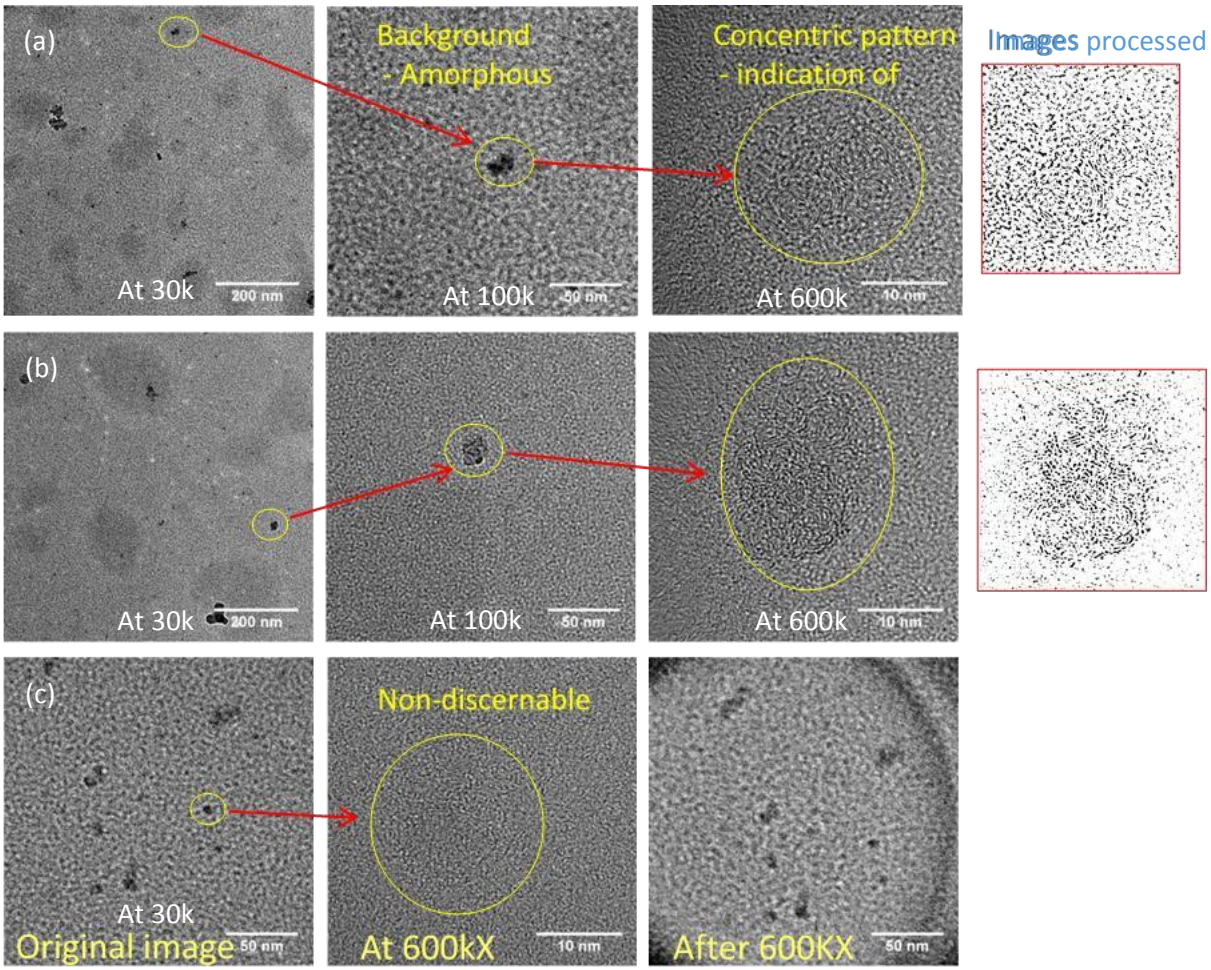

Figure 3.2 (a) and (b) Solid soot nanoparticles with discernable fringes, and (c) young soot or amorphous carbon soot with non-discernable fringes.

Although clear carbon fringe patterns of these sub-23-nm particles were difficult to recognize, there observed many soot particles containing only one single primary particles. These particles are excluded by the current European particle number regulations, because such small soot particles may not be identified from condensed particles by using particle measurement systems. As other researchers also have suggested the existence of soot particles in the sub-23-nm range, it is highly possible to lower the current particle cut-off point of 23 nm to a smaller size in the near future when there will be solid methodologies available that remove all the condensed hydrocarbon particles in the range.

Figure 3.3 shows sizes of primary and aggregate particles measured at different engine operating conditions, based on TEM analysis. Averaged particle diameters were found between 20 nm and 30 nm in the engine load range of 25 to 75% for 1500 and 3000 rpm, which are comparable to those from diesel engines. As the injection timing was varied from 190° bTDC to 330° bTDC, the particle diameter gradually increased from 20 nm to 29 nm. Likewise, the aggregate size also increased from 68 nm to 90 nm in terms of radius of gyration in the same injection timing range. These trends indicate that soot formation process was enhanced with increased residence time of fuel vaporization and fuel-air mixing at the fixed spark timing. Soot oxidation process may have competed with soot formation process with increased

residence time, but soot oxidation may not be active, compared to soot formation during this short period. This is possibly because vaporized fuel was supplied to increase primary particles by the coagulation step within a short period of time and the remaining particles grew further through collisions by the agglomeration step. However, it should be noted that small nanoparticles were missing in measuring primary and aggregate particles, because these would mislead to a wrong conclusion, resulting from large contributions of small sizes.

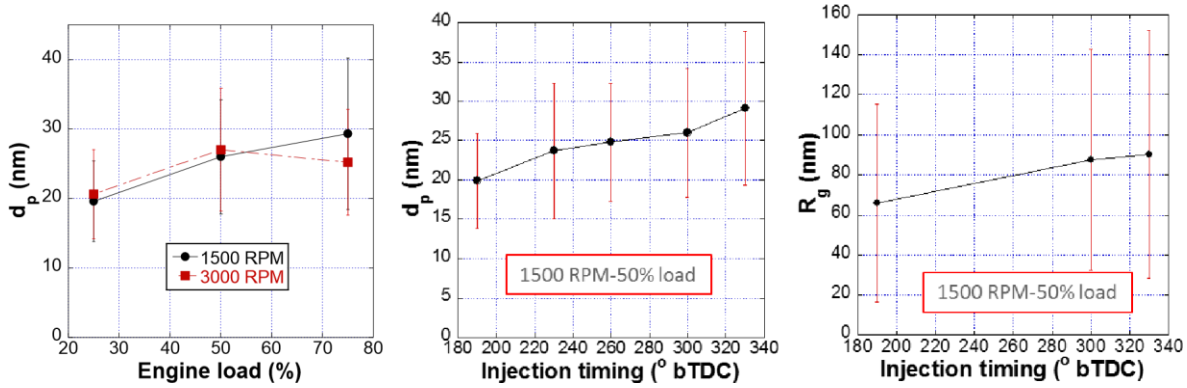

(a) (b) (c)

Figure 3.3 (a) Average primary particle diameters at different speeds and loads for default injection timings, (b) average primary particle diameters at 1500rpm-50% load for varied injection timings, and (c) average aggregate particle sizes in terms of radius of gyration at 1500rpm-50% load for varied injection timings.

Particle size distributions were further examined for these primary and aggregate particles. As shown in Figure 3.4a, it is apparent that with advanced timing, primary particles tend to become larger, resulting in increasing ratios of particles larger than 30 nm in d_p. Therefore, it seems clear that retardation of injection timing facilitate production of small primary particles because of short residence time of fuel vaporization and resultant air-fuel mixing. Aggregate size analysis also shows the trend observed for primary particle sizes, although the trend is relatively less noticeable. Since soot formation process is more pronounced for primary particle growth, the importance of agglomeration process seems to decrease in this range of analysis.

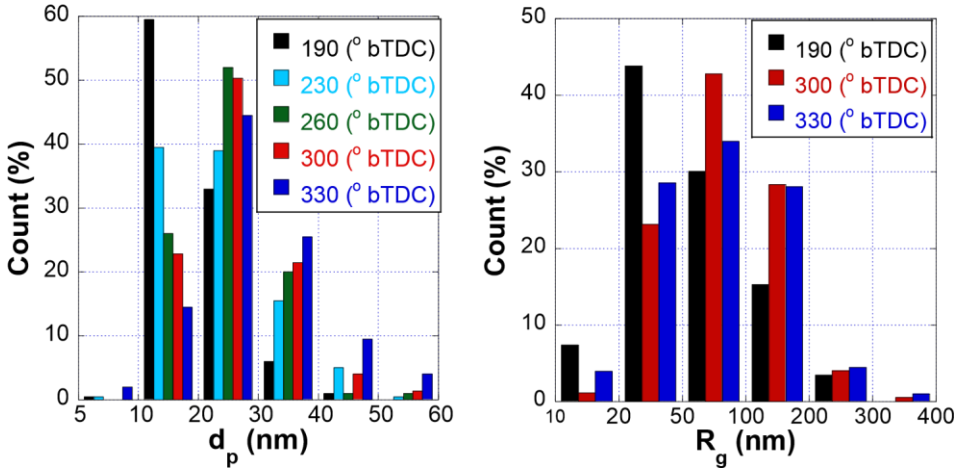

(a) (b)

Figure 3.4 (a) Distribution of primary particle diameters at 1500rpm-50% load for varied injection timings, and (c) distribution of aggregate particle sizes in terms of radius of gyration at 1500rpm-50% load for varied injection timings.

From eqn. (3.4), D_f was calculated as a slope. For numerous aggregate particles from 190° bTDC to 330° bTDC, the range of D_f for GDI particulates was compared with those from other particulates in Figure 3.5. Even though aggregate particle sizes are quite different for different injection timings, the range of the fractal dimension is narrow, indicating that the compactness of aggregate particles is almost similar for these different conditions, in consideration of statistical error within the calculation methodology. This range is located in between light-duty and heavy-duty diesel engines. Therefore, the fractal geometry of GDI particulates could be more compact than light-duty diesel particulates and less compact than heavy-duty diesel particulates, although this conclusion is based on analyzed data at specific operating conditions.

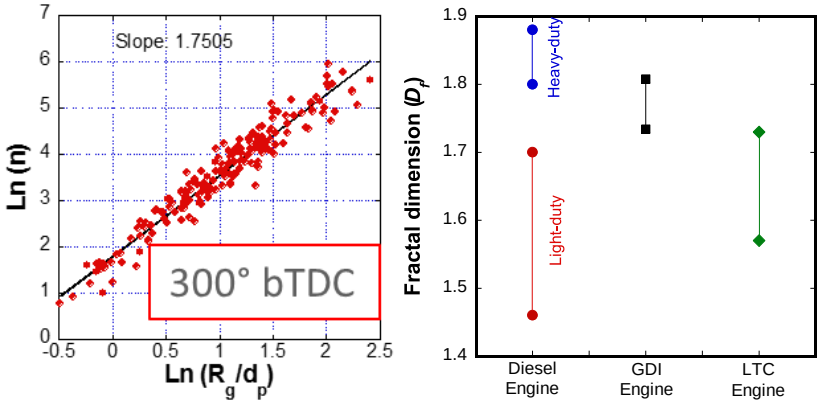

(a) (b)

Figure 3.5 (a) One example of D_f calculation for various aggregate particles: for 300° bTDC at 1500rpm-50% load, and (b) comparison of fractal dimensions for various sources.

GDI nanostructures were also examined for TEM images taken at the magnification of 600,000X. These TEM images were compared for particles from various conditions as well as other particulates that show relatively highly ordered graphite-like structures, as shown in Figure 3.6. As shown in the different GDI particulates, carbon fringe layers surround nucleus on the center of the particle, which is a characteristic of graphite-like structures as others. However, since particle sizes are relatively small at the 1500rpm-25% load condition, carbon fringe layers at this condition appeared to be less organized than other particles. It is typically known that well-ordered carbon crystallites have smooth long carbon fringe layers with reduced tortuosity and the distance between fringe layers is short. In this sense, carbon black is the most ordered and the heavy-duty diesel soot obtained from 1500rpm-50% load is more ordered than GDI particulates. Since raw TEM images are hard to identify these layers, the processed images were compared in Figure 3.7. As found in the images, the selected GDI particulates show crooked fringe layers with interconnections. In comparison, carbon black indicates rare interconnections among fringes and fringe layers are nicely patterned with smooth and long lines, as a good example of well-ordered crystallites.

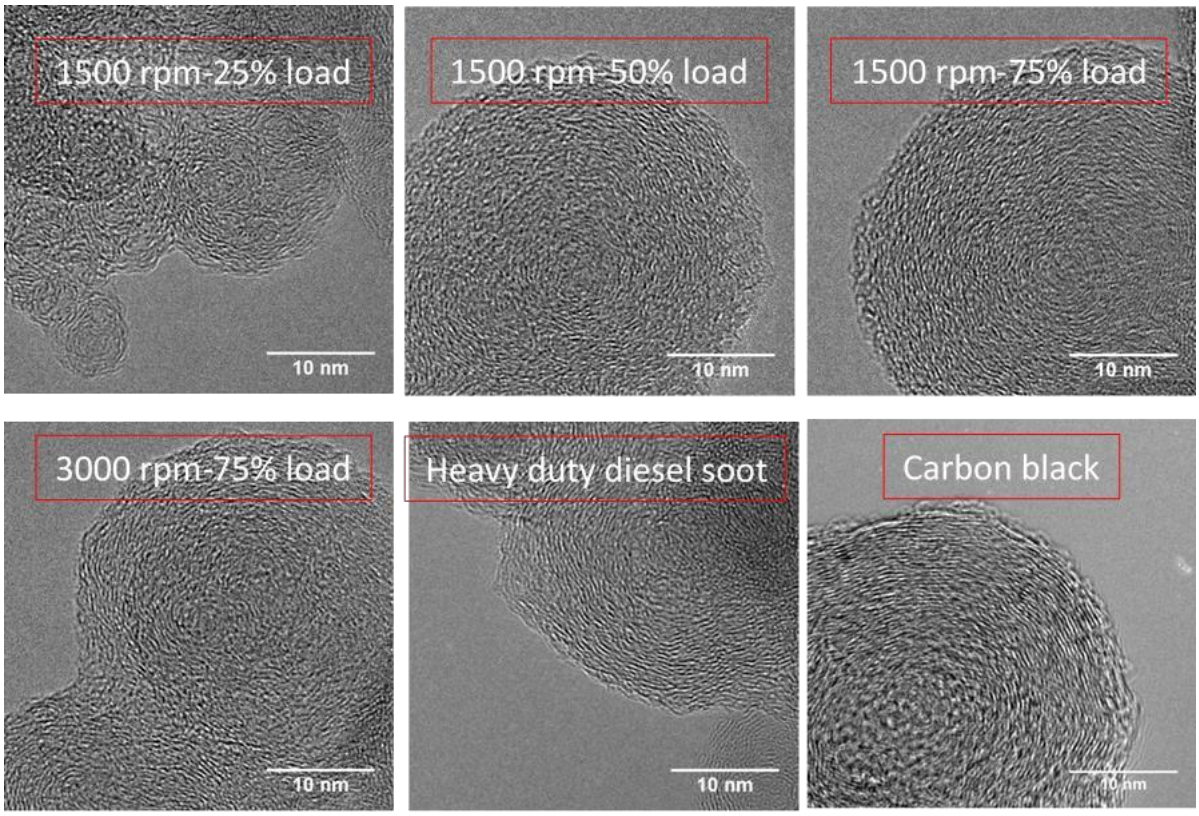

Figure 3.6 HR-TEM images of GDI soot and others taken at 600kX.

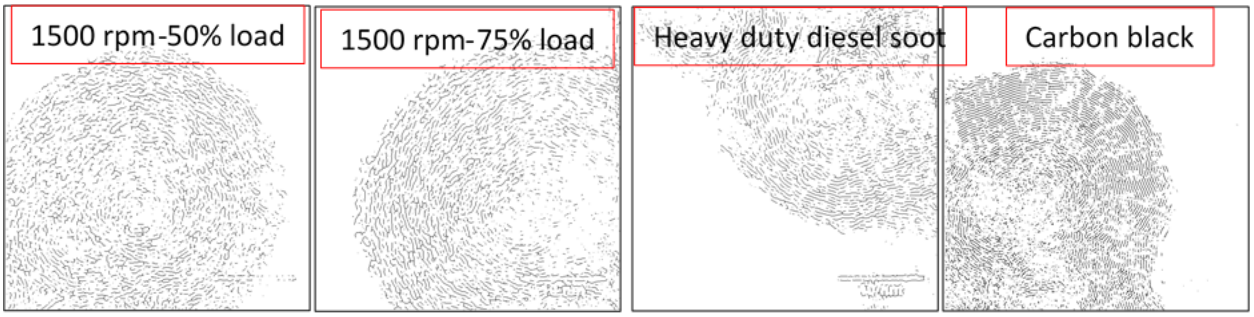

Figure 3.7 Processed TEM images selected from Figure 3.6.

Another interesting observation is that GDI particulates were distorted at high magnifications, resulting from high energy beam. There were no changes noticed on particulates at the magnification of 100,000X during TEM handling. However, some particles were observed to be swollen when the magnification was returned to 100,000X after exposure at the magnification of 600,000X, as shown in Figure 3.8. This is probably because GDI particulates formed at certain operating conditions contained high amounts of hydrocarbons. However, light weight hydrocarbons adsorbed on particulates could have been vacuumed out and they could not have been developed into soot as shown in the images. Therefore, it is assumed that some polycyclic aromatic hydrocarbons (PAHs) absorbed in soot may have exuded and developed into soot at high energy beam. As noted, this type of distortion of particles occurred on particular particles only. Interestingly, this has never happened to conventional diesel particulates as far as our handling has been concerned.

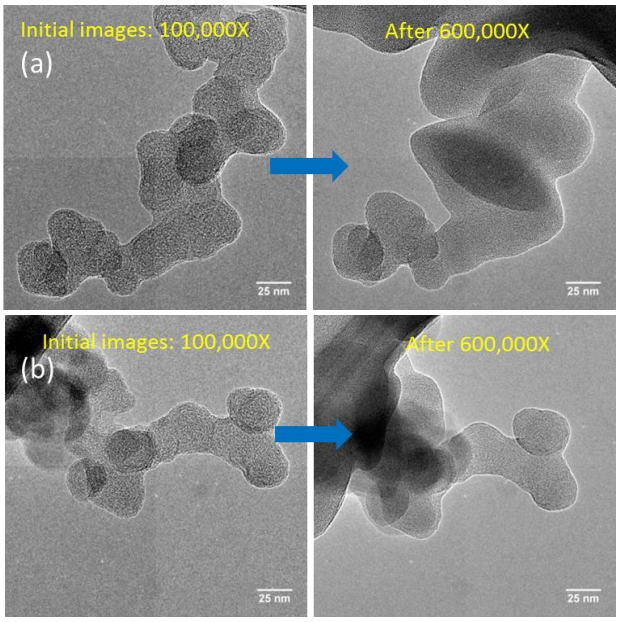

Figure 3.8 TEM images of particles distorted with high electron beam energy.

To better understand carbon crystalline structures at various operating conditions, Raman spectroscopy was performed for different GDI particulates. Figure 3.9 indicates Raman patterns of GDI particulates examined. The D-band at 1360 cm^{-1} is known to be related with disordered carbon, while the G-band at 1580 cm^{-1} corresponds to ordered carbon. As the D-band width becomes narrow and the valley between D- and G-bands at 1500 cm^{-1} gets lowered, carbon crystallites tend to be more ordered. As anticipated from TEM analysis, the diesel soot shows the narrowest D-band width and the lowed valley, indicating this carbon is the most ordered among the samples analyzed. PU as surrogate soot appeared to be a Raman pattern similar to those of GDI soot samples, rather than diesel soot. It is surprising that GDI soot samples were found to be almost identical in pattern. For the better understanding, these peaks were curvefitted with 3 Lorentzian bands and 1 Gaussian band as in the figure and the D1-band was further analyzed in terms of D1 full width at half maximum (D1 FWHM). As shown in the figure, PU and other GDI soot samples are in a similar value range when the statistical deviation is considered. Higher values meant that carbon crystallites are less ordered. According to this analysis, PU and GDI soot encompassing cold idle and medium load soot have almost identical carbon crystalline structures. Therefore, we could conclude that GDI soot samples may have similar carbon crystalline order regardless of operating condition. Since all these samples were taken at stoichiometric conditions except cold idling soot, soot formation process may not be much deviated at the examined conditions. If soot samples are analyzed at extremely lean and rich operating conditions, the result might change.

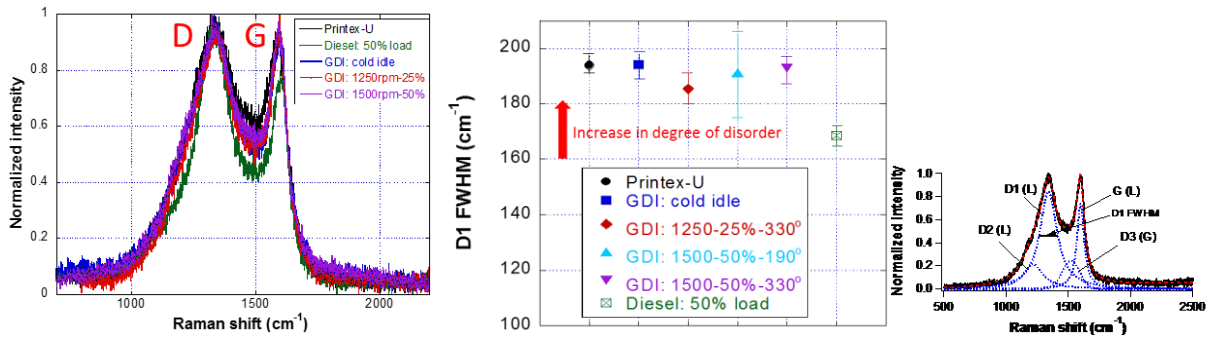

(a) (b) (c)

Figure 3.9 (a) Raman spectra of GDI soot and others, (b) Raman analysis of various soot samples in terms of D1 FWHM, and (c) example of curve-fitted Raman pattern.

Chemical properties of GDI particulates were also examined in terms of surface oxygen functional groups by using Fourier-transformed infrared-attenuated total reflection (FTIR-ATR). As shown in Figure 3.10, GDI and diesel soot samples contained carbonyl C=O, aromatic C=C, aliphatic C-H, C-O-C from ether, and C-O from ester and alcohol in common. Although detailed absorbance patterns are slightly different, the absorbance heights for each one are in a comparable range for GDI and diesel soot. This might explain that diesel and GDI soot contain similar oxygen compounds, despite different fuels used. While GDI soot from the retarded injection at 190° bTDC appeared to contain more aliphatic C-H than do other soot samples, which corresponds to disordered carbon crystallites related with sp^2, it was observed to be ordered in crystalline structure, comparable to other GDI soot according to Figure 3.9. Therefore, this much difference seems not significant when the crystalline structure is concerned. However, it should be noted that according to detailed hydrocarbon speciation by other researchers [3], contents of PAHs and oxygenate compounds in soot were appreciably influenced by fuel types. Despite similarity in the result here, therefore, detailed speciation may lead to a different conclusion.

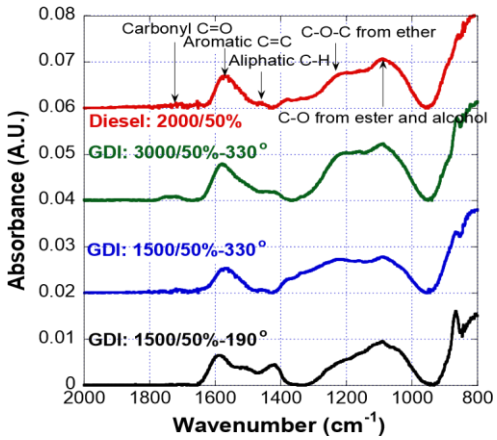

Figure 3.10 FTIR-ATR analysis of various soot samples showing surface chemistry.

3.2 Soot emissions analysis

Since soot emissions from GDI engines are known to be significantly affected by engine operating conditions, soot mass and number emissions were measured with varying conditions by using a micro soot sensor and SMPS, respectively. In Figure 3.11a, soot mass emissions

were compared for cold steady, cold transient, hot steady and hot transient conditions. These operating conditions are defined as follows: hot steady was operated at 1500rpm-25% load over coolant temperature of 60 °C, hot transient was accelerated from 1000 rpm to 3000 rpm with full throttle open over coolant temperature of 60 °C. In comparison, cold steady & transient were operated at the same conditions as hot steady & transient when the coolant temperature was lower than 60 °C. Figure 3.11a indicates that cold conditions obviously produced more soot emissions, so cold transient produced 50 times more soot mass than hot steady. To better understand soot emissions, the particle number distribution was examined while engine coolant was warmed up as shown in Figure 3.11b. It is apparent that the number decreased significantly with coolant temperature, so when the coolant was fully warmed at 82 °C, the number emissions were reasonably low. Correspondingly, soot mass emissions also decreased significantly with coolant temperature. Since fuel wetting influences soot production rate, it is clear that soot formation was suppressed as chamber got warmed.

Two different cases were compared by monitoring soot accumulation in filter as shown in Figure 3.12. With rapid acceleration filter pores already had much soot loading with only 30 seconds, while at hot steady filters pores had a negligible amount of soot loading

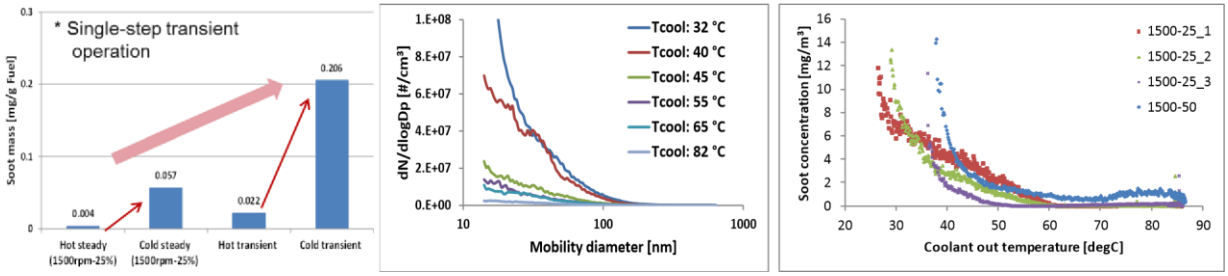

(a) (b) (c)

Figure 3.11 (a) soot mass concentration at transient and steady conditions, (b) variation of particle size distribution with increased coolant temperature, and (c) variation of soot mass concentration with increased coolant temperature.

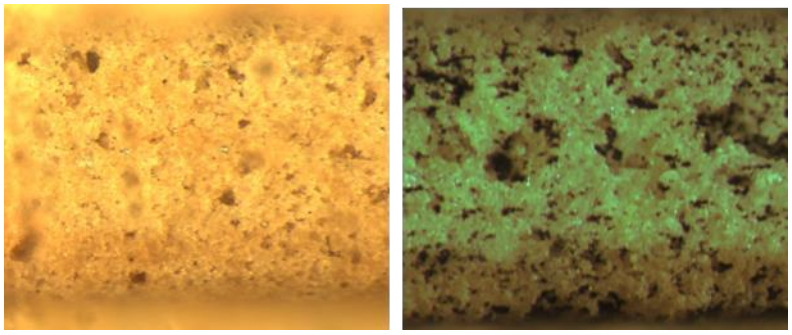

(a) (b)

Figure 3.12 (a) Hot steady for 90 seconds at 1500rpm-50% load, and (b) cold transient for 30 seconds when the engine was rapidly accelerated from idling to 1500rpm-25% load.

Soot mass emissions were also examined during fuel-cut operations as shown in Figure 3.13. Although there was no combustion occurring during fuel-cut, sharp peaks of soot emissions were observed as marked as dotted circles. It is clearly seen that when the soot emissions were higher during the transient operations right before the fuel-cut, they tend to increase during the fuel-cut. Thus, soot mass emissions were lower at the coolant temperature of 70 °C than at 50

°C. Since much amounts of soot may have been accumulated on piston top land and in cylinder and exhaust pipes during transient modes, they seem to emit with lubricant oil during fuel-cut by reverse blow-by process and detachment of accumulated soot. As found in Figure 3.13c, soot mass emissions during fuel-cut is well correlated with total soot mass emissions and the first accounts for 2 – 6% of the latter.

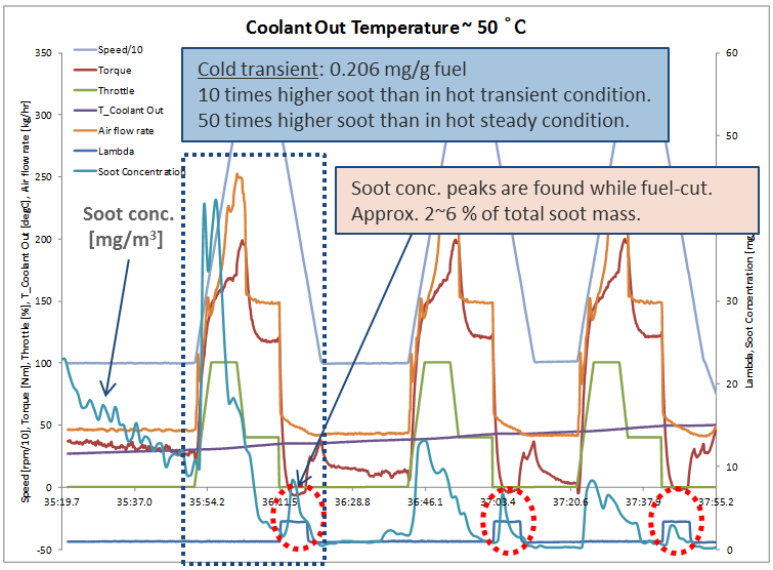

(a)

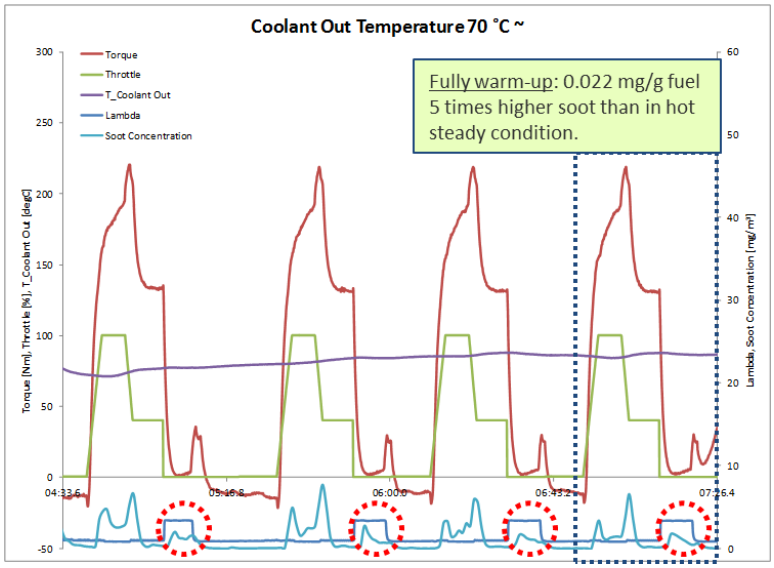

(b)

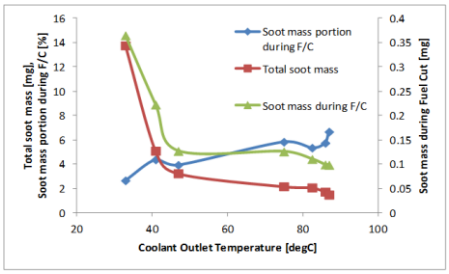

(c)

Figure 3.13 Soot mass emissions during transient and fuel-cut modes with varying coolant temperature: (a) coolant temperature at 50 °C, (b) coolant temperature at 70 °C, and (c) comparison of total soot mass and soot mass during fuel-cut as a function of coolant temperature. Increased soot formation at cold-idling condition can be ascribed to increased rich fuel regimes and delayed fuel-air mixing, resulting from fuel wetting. In order to simulate soot formation process, impacts of fuel injection timing on soot emissions were investigated. Figure 3.14 shows soot emissions at 1500 rpm as examples. While soot mass emissions were extremely low at optimized injection timings as default settings, they were enormously high at advanced fuel injection. Although retarded fuel injection produced increased particles in the

sub-40-nm range, which was anticipated from TEM analysis, particles larger than 40 nm in mobility diameter were heavily produced with advanced fuel injection as shown in Figure 3.14b. Since advanced fuel injection created wall & piston wetting, especially in 50% and 75% load conditions, soot emissions were enormously high like fuel wetting at cold -idling condition.

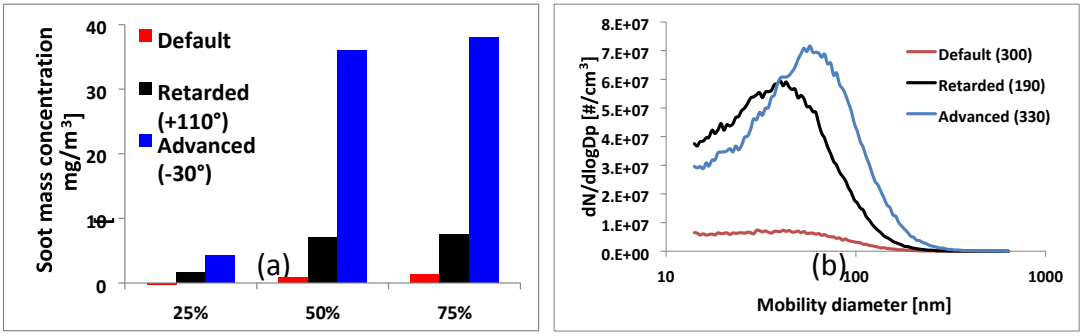

Figure 3.14 Soot emissions at 1500rpm with varying injection timing: (a) Soot mass concentration at different loads, and (b) particle size distribution at 50% load.

Soot mass emissions were further examined for 3000 rpm to compare with those for 1500 rpm, as found in Figure 3.15. Soot mass emissions were extremely low at 300° bTDC as the optimized fuel injection timing for both 1500 rpm and 3000 rpm. Soot mass emissions significantly increased at 1500 rpm for 190° bTDC. Interestingly, soot mass emissions were extremely high at 3000 rpm for the same injection timing. Since fuel vaporization and fuel-air mixing were limited with much amounts of fuel injected, soot formation process was significantly enhanced even with retarded fuel injection. As explained early, soot mass emissions were extremely high at 330° bTDC, especially at 50% and 75% load conditions for 3000 rpm as well as 1500 rpm, due to wall and piston wetting. Because soot formation is also dependent on cylinder temperature and other factors, soot mass emissions from 3000 rpm did not exceed those from 1500 rpm.

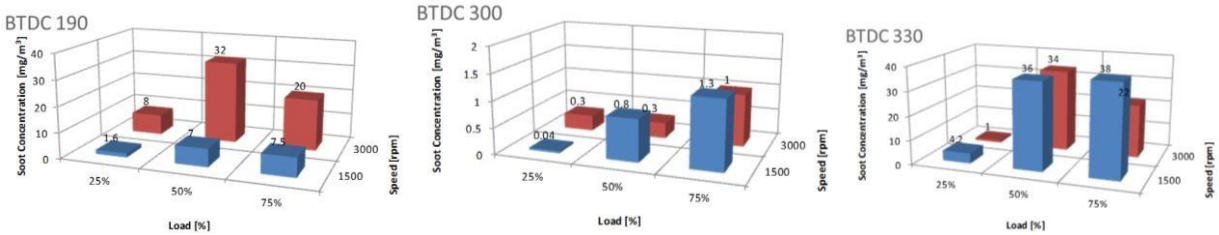

Figure 3.15 Comparison of soot mass concentration at 1500 rpm and 3000 rpm for different loads with varying injection timing.

In order to evaluate the removal of particulate emissions by the TWC converter, soot mass and number emissions were measured in the upstream and downstream of the converter at various operating conditions. As shown in Figure 3.16, 1 and 2 represent low space velocity conditions, 3 and 4 do medium space velocity conditions and 5 corresponds to high space velocity conditions, in consideration of exhaust gas temperatures and intake air flow rates. When the space velocities were low, particle numbers drastically decreased in the entire range of particle emissions. When the space velocities were medium, however, the particle reduction was only

noticeable at the sub-40-nm range. In comparison, when the space velocity was high, the reduction occurred on particles below 40 nm and over 60 nm. The reduction of small particles is the effect of diffusion of nanoparticles. The reduction of particles in accumulation mode is related to impact by particle collisions. So, the particle reduction in the different size range is because these diffusion and impact effects occur differently in combination with exhaust flow rates.

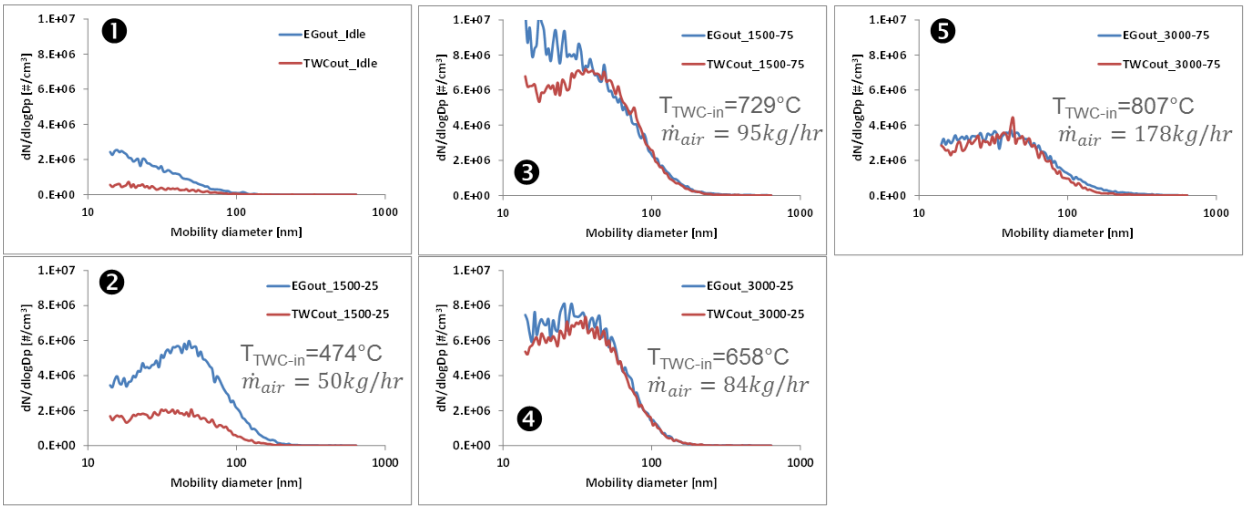

Figure 3.16 Particle size distributions before and after TWC in variation of exhaust flow rate.

Effects of particle reductions were summarized in Figure 3.17 by mass and number emissions, respectively. Particle mass reduction was significant with low and high space velocities (the effect in 1 is not noticeable because the total emissions were too low for comparison), while it was minor with medium space velocities. In comparison, particle number reduction was obvious for all the examined cases. In particular, the effect was observed to be more apparent at low space velocities (approximately 60-75% reduction) because small nanoparticles were filtered in the converter by the diffusion process. Although the effect was marginal, TWC could still reduce approximately 10% at medium and high space velocities.

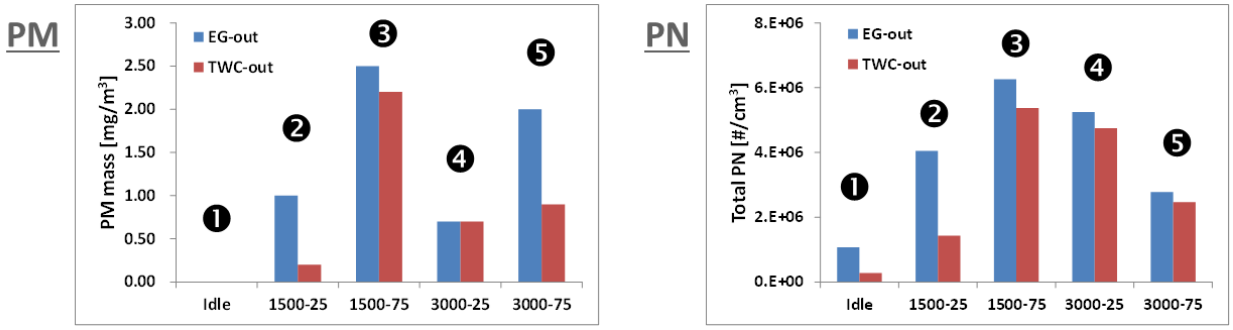

Figure 3.17 Comparison of PM mass and number reductions with TWC at various flow rates.

PM samples collected in the upstream and downstream of the TWC converter were analyzed by TGA and scanning electron microscopy (SEM). The engine was operated at 1500rpm-50% load for 330° bTDC. First, volatile organic fraction and ash fraction in soot were measured after the samples were pretreated in the TGA at 600 °C for 1 hour. As shown in Figure 3.18a, the sample taken from the upstream of TWC contained VOF of 6.79% and ash of 0.07%, while that taken from the downstream had 5.94% and 1.10%, respectively. This indicates that some volatile hydrocarbons in soot were evaporated while passing the converter. Also, there was a

contribution of TWC to ash fraction. When elemental analysis was performed in SEM for both samples, the pre-TWC sample showed Ca, P, Zn, Na, S and others, which are typical engine-oil additives, as found in Figure 3.18b. In comparison, the post-TWC sample contained Mg and Si in addition to additive residues. This means that some wash-coating materials were separated from TWC during the engine operation. Since the portion of active catalysts such as PGM is low in washcoating materials, this elemental analysis could not provided PGM as components.

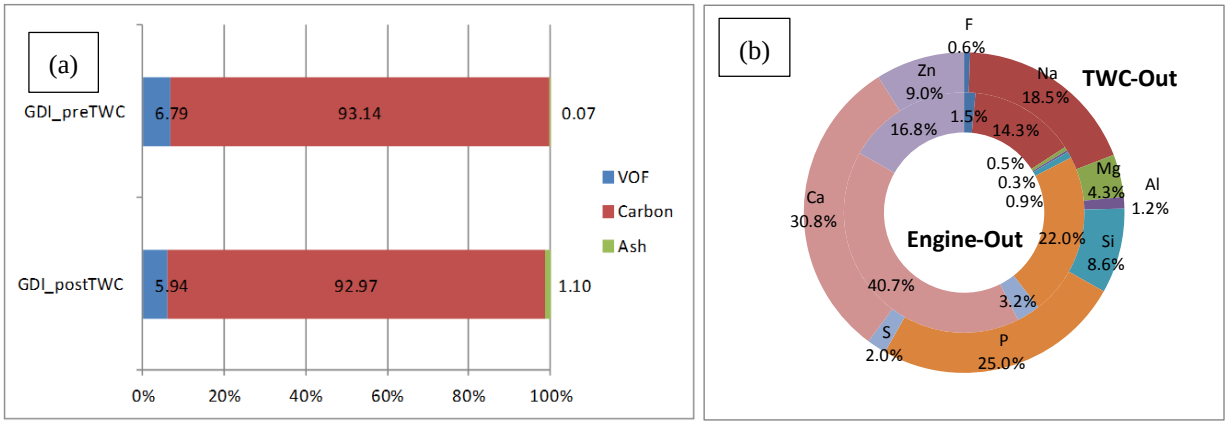

Figure 3.18 (a) VOF and ash fraction before and after TWC from TGA tests, and (b) SEM-EDS analysis of engine-out ash and post-TWC ash.

3.3 Evaluation of oxidative reactivity of GDI soot

GDI particulates were taken at various operating conditions and soot mass concentrations and ash fractions were analyzed. For the soot mass concentration measurements, the AVL micro soot sensor was used and ash fractions in soot were measured from the remaining residues after soot burning in TGA. As shown in Figure 3.19, for various GDI soot samples, there was an interesting correlation observed between soot concentration and ash content. When soot mass concentration is high, ash fraction in soot is relatively small. Although engine-oil consumption is dependent on engine operating conditions, the contribution of ash containment in soot formation is assumed to be similar. In that case, ash fraction in soot is inversely correlated as soot formation increases. Although soot emissions from this engine were intentionally increased by advanced fuel injection, they were typically below 1 mg/m^3 at default injection timings. Therefore, ash fraction is expected to be higher than 1.5% as indicated as the GDI operation regime. As a good example, the GDI sample obtained at 1250rpm-25% load contained ash fraction of almost 3.5% at the default condition.

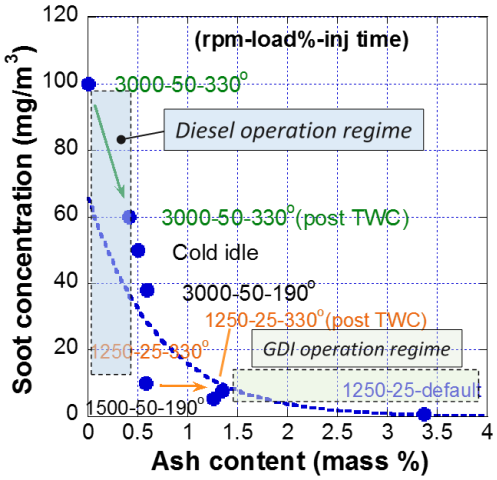

Figure 3.19 Relation between ash content and soot mass concentration.

For these samples containing different ash fractions, TGA experiments were performed to understand ash impacts on soot oxidation. As shown in Figure 3.20a, soot oxidation was completed faster with increased ash fraction. Indeed times required to oxidize 50% and 90% of soot decreased with increased ash fraction, indicating that soot oxidation was enhanced with ash present.

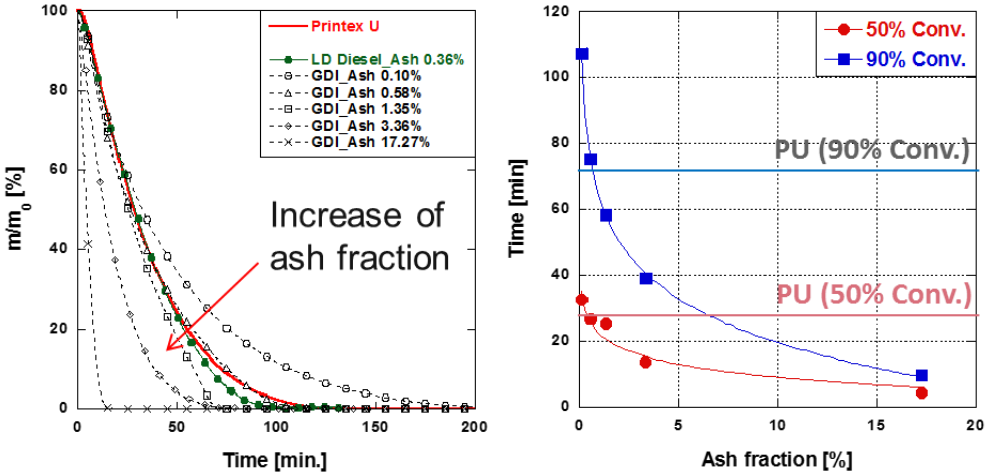

(a) (b)

Figure 3.20 (a) TGA experiments at 600 °C with 8% O_2 in N_2, and (b) Times measured at the conversions of 50% and 90% as a function of ash fraction.

In order to analyze ash contribution to soot oxidation characteristics, soot oxidation rates were calculated for different soot samples examined as a function of conversion, in Figure 3.21. The patterns of soot oxidation rates are characterized with A, B and C. In the case of GDI soot samples, soot oxidation rates rapidly increased with conversion in the late stage as ash fraction increased. However, the sample containing the least ash fraction did not show sharp increase in the rate like PU. However, the light-duty diesel soot showed rapid increase in the rate despite low ash fraction. Therefore, the increasing pattern of the rate seems to be related to the properties of soot samples. As far as GDI soot is concerned, the increase in ash fraction contributed to the increase in the rate at the late oxidation stage. In addition, soot oxidation rates were found to be high even at the initial oxidation stage. Since soot oxidation would preferentially occur on disordered carbon crystallites as well as soluble organic fraction within

soot survived after volatilization, the increase in the rate at the initial oxidation stage was thought be caused by the contribution of those SOF and disordered carbon crystallites such as weakly bonded carbon (WBC). In consideration of these properties, soot oxidation rates were described to make an oxidation model as indicated in Figure 3.21b. The intrinsic carbon soot oxidation rate was obtained from carbon oxidation at "B" stage for the GDI soot containing the least amount of ash, and the carbon oxidation rate assisted by Ash_C was obtained from the shift of the intrinsic carbon soot oxidation rate, because soot oxidation rate was observed to upshift as ash fraction increases. As explained early, shades in the initial and late oxidation stages were contributed by SOF/WBC and ash fraction, respectively.

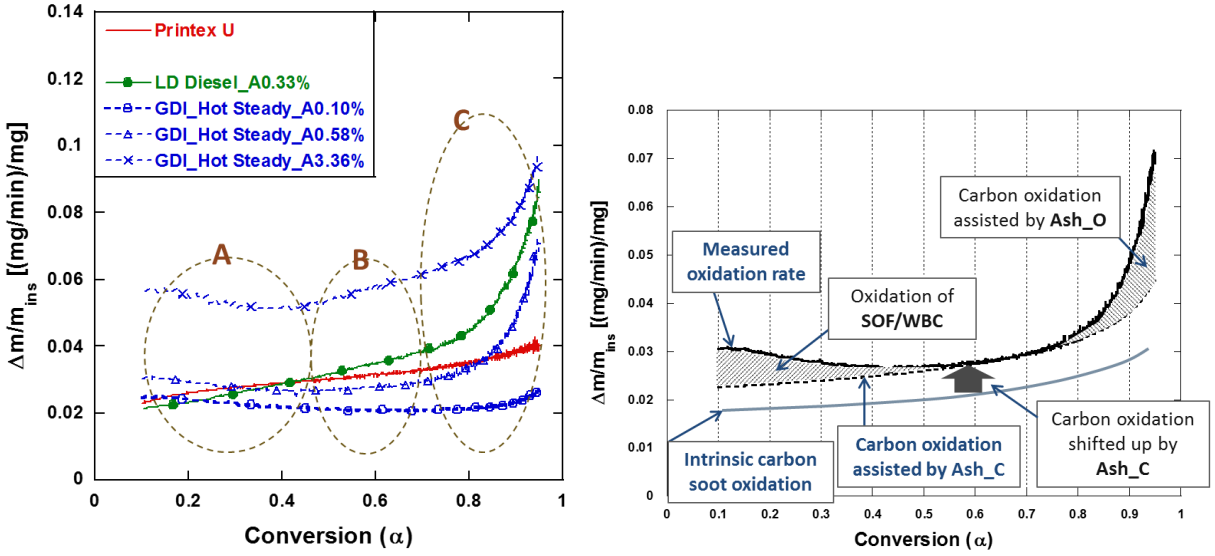

(a) (b)

Figure 3.21 (a) Instantaneous reaction rate with conversion for various soot samples, and (b) schematic of a modified kinetic model for instantaneous reaction rate with conversion.

Previous studies of the reaction kinetics of carbonaceous soot have reported that the Arrhenius-type equation in Eq. (3.1) is well accepted for the temperature dependence of soot oxidation by oxygen,

$$r = \frac{d\alpha}{dt} = A \times e^{-E_a/RT} \times (1-\alpha)^n \quad (3.1)$$

where r is the rate of reaction (s^{-1}), A is a pre-exponential factor (s^{-1}), E_a is activation energy (kJ mol^{-1}), R is the universal gas constant (kJ mol^{-1} K^{-1}), α is the degree of conversion, and n is reaction order. However, GDI soot oxidation rates were not accurately predicted by this conventional kinetic model, as ash contribution is relatively high as indicated in Figure 3.22. Accordingly, a modified kinetic model encompassing ash and SOF/WBC contributions was developed and the results show that it could well predict soot oxidation rates for isothermal and non-isothermal conditions. The modified kinetic model and parameters used were summarized in Tables 3.1 and 3.2

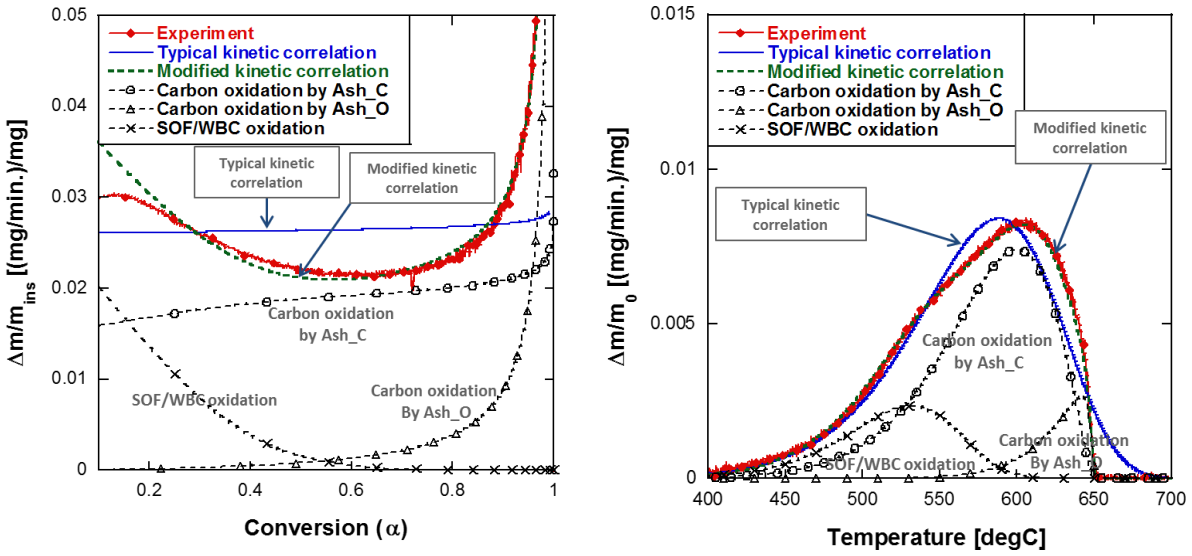

(a) (b)

Figure 3.22 Examples of modified kinetic correlations with each component involved for (a) isothermal soot oxidation at 600°C, and (b) non-isothermal soot oxidation.

Table 3.1 Modified kinetic correlation for GDI engine soot.

	Formula
Overall reaction rate	$r = \frac{d\alpha}{dt} = (m_{S-W,0}/m_{soot,0}) \cdot r_{S-W} + (m_{C,0}/m_{soot,0}) \cdot r_C$
SOF/WBC reaction rate	$r_{S-W} = \frac{d\alpha_{S-W}}{dt} = A_{S-W} \times e^{-E_{a,S-W}/RT} \times (1-\alpha_{S-W})^{n_{S-W}}$
Carbon reaction rate	$r_C = \frac{d\alpha_C}{dt} = A_C \times e^{-E_{a,C}/RT} \times (1-\alpha_C)^{n_C} + (1-\alpha_C) \cdot (a \cdot \exp(b \cdot T)) \cdot f_{ash\_O,i}$

Table 3.2 Kinetic parameters of carbon oxidation with combustion-derived ash effects.

	Parameters
A_{S-W}	1,646,232.7
$E_{a,S-W}$	147.26

$n_{S\text{-}W}$	1.0377	
A_C	491,884.9	
$E_{a,C}$	$E_{a,C} = -1.169 \times f_{ash\_C}$ [%] + 152.5	
n_C	$n_C = -0.1854 \times f_{ash\_C}$ [%] + 1.0047	
a	5.70069E-11	b 0.0255525

As indicated in Figure 3.23, engine oils for gasoline and diesel engines contain Ca, P, Zn, Na, Mg, Mo and etc., whose compositions are different depending on the type. In particular, Ca, Zn and P are major components in common. Based on these ICP results, possible additive compounds of Ca, Zn and P were identified as Ca sulfonate, Phosphite and Zinc dithiophosphate. Since non-detergent oil contains low amounts of Ca, Zn and P, it was mixed with individual additive compounds to formulate Ca-, P- and Zn-P-specific engine oils as shown in Table 3.3. Then, 1% of these additive specific engine oils were mixed with gasoline for burning in the engine and additive-specific soot samples were obtained for TGA experiments.

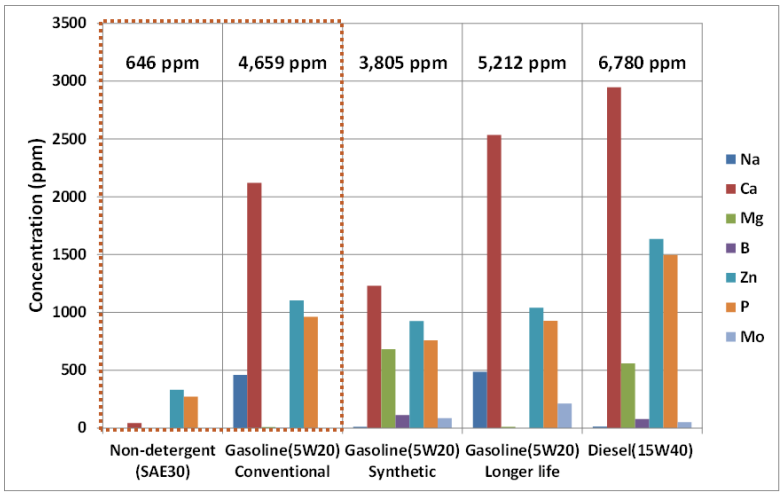

Figure 3.23 ICP analysis of various engine oils.

Table 3.3 Compositions of additives in formulated engine oils.

Dosage in fuel (ppm)	Ca	Zn	P	Na	Total
Gasoline Only	0	0	0	0	0

1% Non-detergent oil	0.4	3.3	2.7		6.4
1% Conventional oil	21.2	11.0	9.6	4.6	46.6
Calcium Sulfonate in 1% non-detergent oil	4 – 24	0	0	0	4 – 24
Phosphite in 1% non-detergent oil	0	0	18 – 55	0	18 – 55
Zinc Dialkyl Dithiophosphate (ZDDP) in 1% non-detergent oil	0	8 – 206	8 – 191	0	16 - 397

Figure 3.24 shows soot oxidation results performed by TGA at 600 °C with 8% O_2 in N_2. Compared to the soot oxidation pattern of soot derived from non-detergent oil as a reference, oxidation of soot derived from conventional oil was significantly enhanced. Soot oxidation was proportionally improved with the increase in ash fraction. Soot derived from Ca compounds also showed enhanced oxidation. Even though the ash fraction was much lower, soot with Ca ash of 5.8% had a similar oxidation pattern of soot with ash of 23.4% derived from conventional oil. However, soot samples containing P and Zn ash showed opposite trends to those with ash from conventional engine oil and Ca additive, so soot oxidation was retarded with P and Zn presence. These trends are well described in Figure 3.24b as T90 because soot oxidation reactivity is in good agreement with T90. Accordingly, it is clear that the reason why soot oxidation reactivity was enhanced with the presence of ash is that since Ca additive is the most abundant in oil additives, Ca effects dominate soot oxidation, rather than effects of lower amounts of other components.

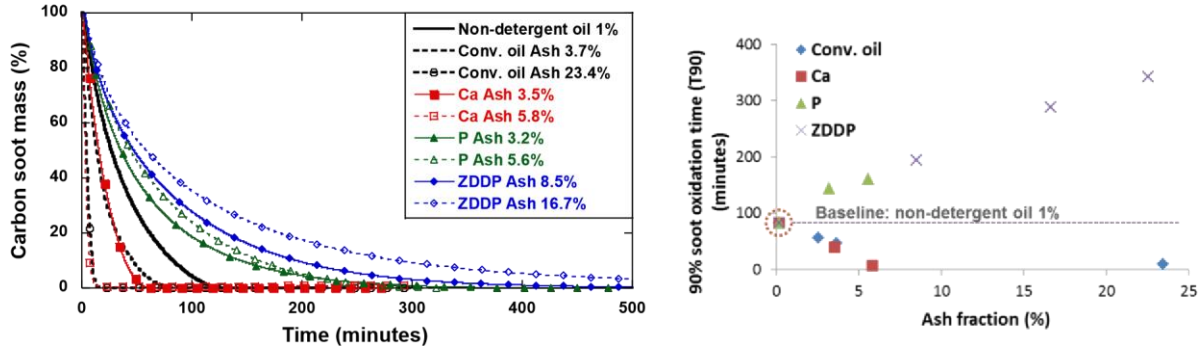

(a) (b)

Figure 3.24 TGA results of additive-specific soot samples at 600°C with 8% O_2 in N_2: (a) TGA oxidation curves, and (b) T90 as a function of ash fraction.

To identify chemical compounds of ash derived from Ca sulfonate, synchrotron X-ray powder diffraction was performed in Advanced Photon Source at Argonne National Laboratory. Ash derived from Ca dodecyl-benzene sulfonate was recognized to be $CaSO_4$ according to compounds searching software. Indeed $CaSO_4$ from Aldrich-Sigma showed peaks at identical degrees of 2θ with larger intensities as ash in Figure 3.25. Since Ca dodecyl-benzene sulfonate contains Ca_2^+/SO^-_3 structure, ash was formed with $CaSO_4$ after detaching benzene and the

connected hydrocarbon chain during oxidation process. In previous studies, $CaSO_4$ was also identified to be a major chemical compound among ash components.

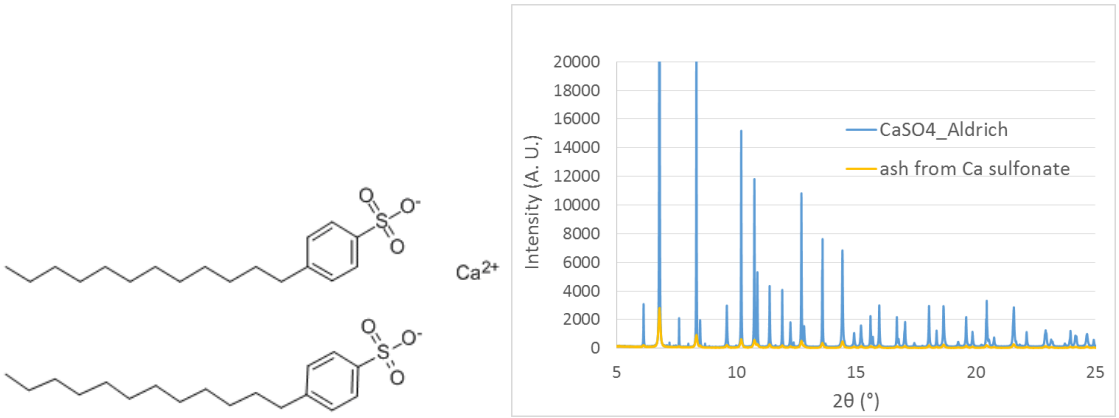

Figure 3.25 Chemical forumula of calcium dodecyl-benzene sulfonate and comparison of synchrotron XRD peaks of $CaSO_4$ and ash derived from Ca sulfonate.

Figure 3.26 shows TGA results of PU oxidation in the presence of various chemical compounds. For the tests, mixtures of PU and each chemical were grinded in an agate mortar for tight contact.

$CaHPO_4$, potential ash chemical, CaS and CeO_2 were chosen for references. $CaSO_4$ from SigmaAldrich and drierite were compared as the same $CaSO_4$ to understand effects of surface area, because the former has 2 m^2/g and the latter has 10 m^2/g. As shown in the figure, drierite has a bigger impact on soot oxidation than does $CaSO_4$ from Sigma-Aldrich, contributed from improved surface area. CaS and drierite containing $CoCl_2$ showed remarkable results, but they were found to be unstable after the test because they were oxidized at high temperatures. $CaHPO_4$ is shown to be minor in influence, so indeed this material is not a contributor to improved soot oxidation. As discussed early, Ca-derived ash showed a remarkable improvement in soot oxidation. According to SMPS analysis with other engine oils, particles in the sub-100-nm range were significantly produced. Therefore, it is assumed that Ca-derived ash particles emitted from the engine are also nanoparticles in a similar size range as above, resulting in increased surface are. As a result, Ca-derived ash particles with high surface area could show an improved soot oxidation reactivity, in comparison to $CaSO_4$ available in market.

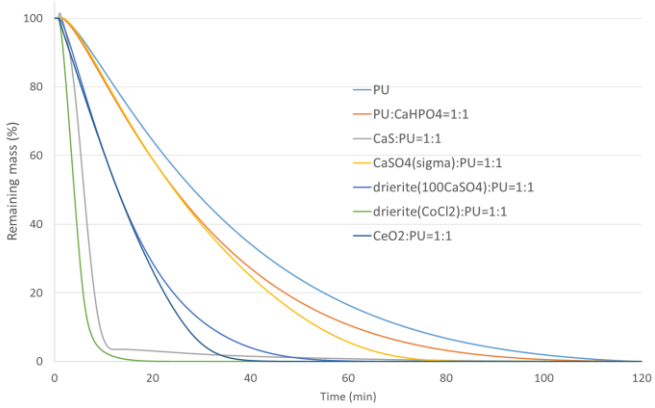

Figure 3.26 TGA results of soot oxidation in the presence of chemicals at 600 °C with 8% O_2 in
N_2.

The role of sulfur was examined by using XANES in APS-ANL. XANES can identify sulfur oxidation states, so it is of great interest if they vary during soot oxidation. In Figure 3.27, $CaSO_4$_fresh is drierite, $CaSO_4$_50% is a sample remained after 50% of PU was oxidized with PU/drierite mixture, and $CaSO_4$_100% is a sample remained after all the PU was fully oxidized with PU/drierite mixture. As found in the figure, the XANES curves were slightly different, which could suggest that these sulfurs are not in exactly same coordination. The peak at 2480 keV indicates 6+, resulting from $CaSO_4$. From the detailed patterns, $CaSO_4$_fresh was found to be $CaSO_4 \cdot 1/2H_2O$ and $CaSO_4$_50% and $CaSO_4$_100% were anhydrous $CaSO_4$ without water. More importantly, $CaSO_4$_50% had a small hump at 2471.4 keV. According to the literature survey, this peak occurs when sulfur oxidation state is 1+. Since $CaSO_4$_100% did not have this peak, the result may indicate that $CaSO_4$ was converted to some chemicals with sulfur oxidation state of 1+ during soot oxidation. The similar result was verified with another sulfate material. There could be more vigorous chemical shifts during soot oxidation, but these changes may not be found with ex-situ measurements because unstable chemical states may have quickly converted into stable states in air, even though they existed.

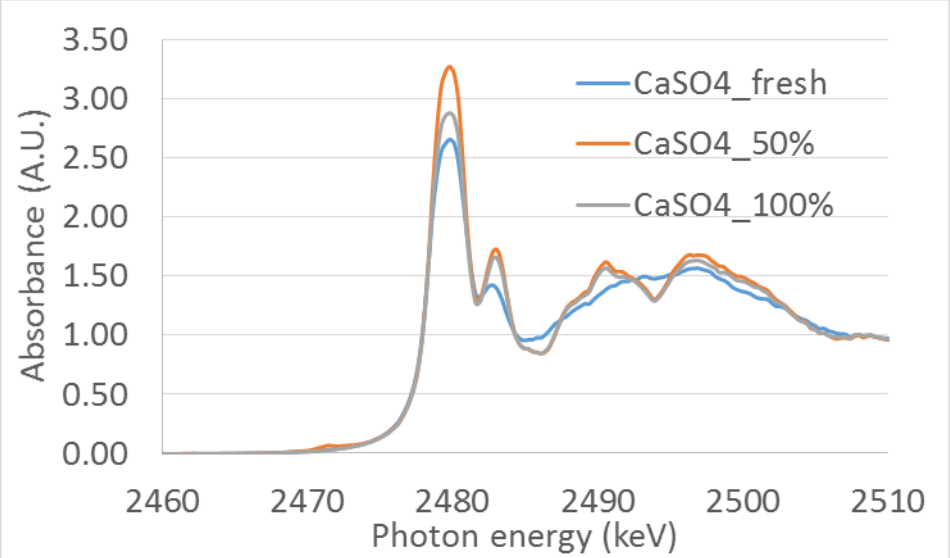

Figure 3.27 XANES analysis of $CaSO_4$ to examine sulfur oxidation states.

3.4 Evaluation of filtration and regeneration processes in the visualization set-up

Filtration was performed with an AC 200/12 bare filter at the inlet temperature of 200 °C. The soot mass concentration remained at 2.5 mg/m^3 when the engine was operated at 1500rpm-25% load. The peak number of particles was measured to be 8x10^6/cm^3 in the upstream of the filter and it decreased dramatically in the downstream of the filter from the starting point, achieving 74% number filtration efficiency. The efficiency was gradually improved and reached the stable point at 97% in 50 min. As shown in Figure 3.28, even with this relatively long process, filtration process was still in the depth filtration regime because soot mass emissions were low. Although pressure drop gradually increased, filtration efficiency was saturated at around 43 min before all the pores were plugged with particles. The Greenfield gap where particle penetration occurs mostly was evaluated in the starting point only as an example, because size-dependent filtration efficiencies reach max points with time. As shown in the figure, particles in the range of 60 to 100 nm penetrated the filter mostly with the number filtration of 60 –

70%. This size range is lower than that examined by PNNL using aerosol particles, probably because gas velocity, soot concentration and morphology will affect filtration mechanisms. However, it is interesting to note that GDI particles in the small range may escape filters, so it might be necessary to understand if these small particles penetrated can cause any additional harmful effects, compared to larger particles.

Continuous regeneration was also performed for the filter after a certain amount of soot was loaded. As indicated in Figure 3.29, soot loading was not observed even after 50 min at the default injection timing for 1500rpm-50% load. With advanced injection timing, however, soot cake was achieved within 10 min like diesel engine case. Accordingly, the experimental steps were taken as follows: for soot cake formation, fuel injection was advanced at 330° bTDC for 1500rpm-50% load. When soot loading in filter was enough to have soot cake, fuel injection was retarded to a default injection timing of 300° bTDC. As shown in Figure 3.30, O_2 and NOx concentrations were 0.28% and 11ppm, respectively, at the inlet point of the filter and the exhaust temperature was 500 °C. As shown in the plot, pressure drop decreased slowly from 2.6 kPa to 2 kPa, so it seems continuous regeneration occurred even with low concentrations of O_2 and NOx at 500 °C. Increased temperatures would facilitate regeneration process, but they could not be examined with this set-up, because insulation was not enough for this long bypassed line from the main exhaust pipe. Accordingly, more experiments were performed with a new bench flow reactor as explained in the following section.

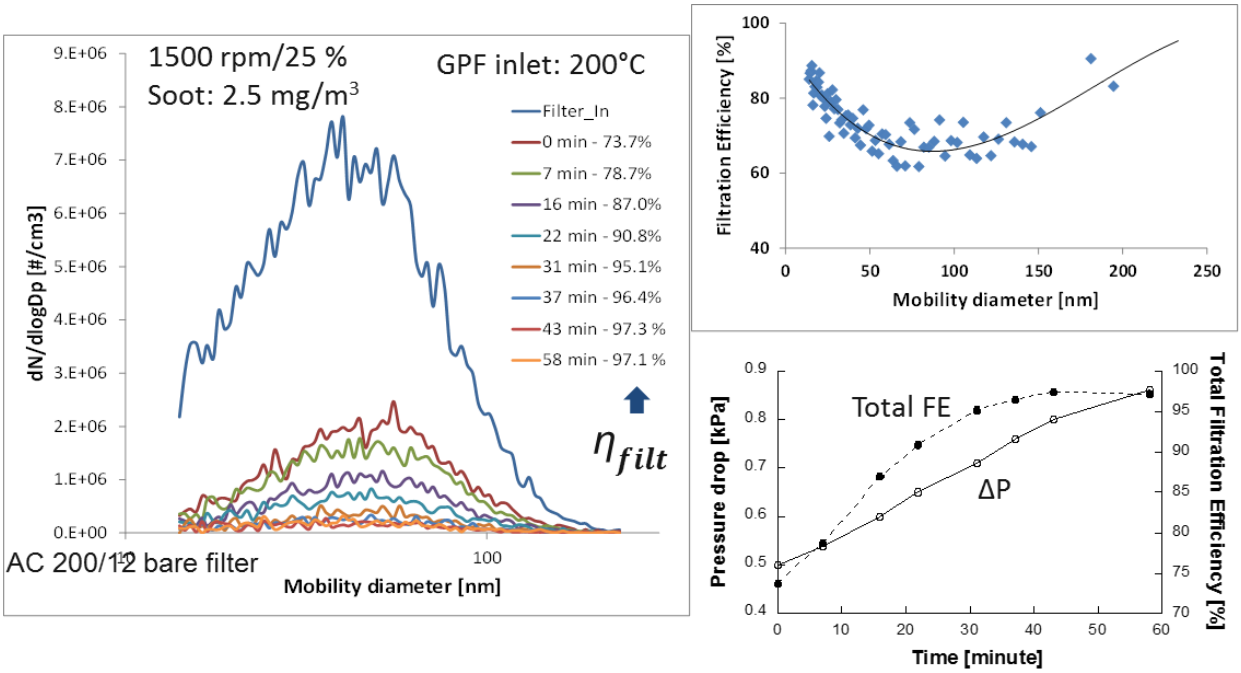

Figure 3.28 Particle size distributions with time, initial filtration efficiency and variations in pressure drop and total filtration efficiency with time by soot loading.

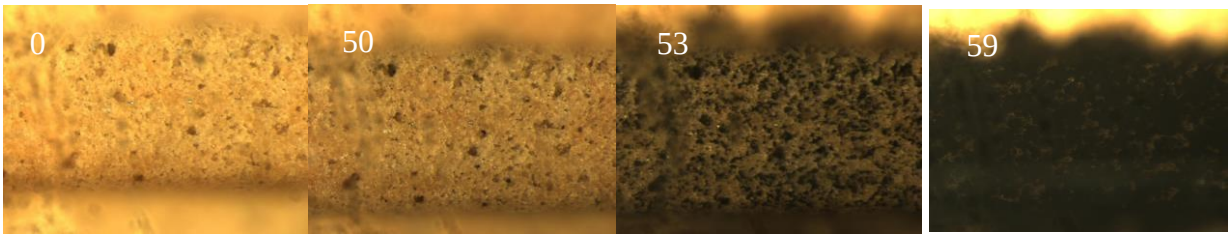

Figure 3.29 Filter visualization during filtration process (the default injection timing between 0 and 50 min and the injection timing was switched to the advanced timing of 330° bTDC at 50 min).

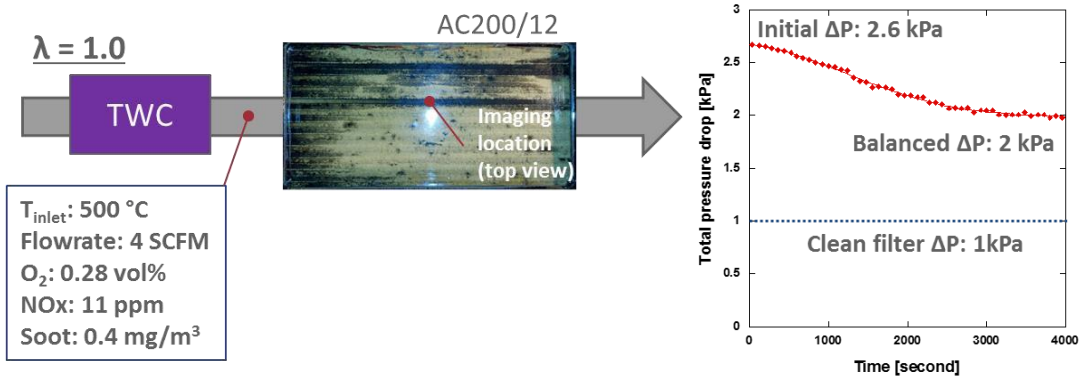

Figure 3.30 Filter regeneration condition, top view of the filter and pressure drop change with time by regeneration process.

3.5 Evaluation of filtration and regeneration processes in the bench-scale flow reactor Although bare filters provided fundamental understandings of filtration and regeneration processes, they cannot inform actual test results in GPF systems because catalyst coating is typical for GPF use. Since TWC has already been employed in GDI engines, they have been conventionally coated on GPFs. These TWC-coated GPFs have been configured in many types such as add-on GPF (TWC and TWC-GPF separated) or integrated GPF (TWC-GPF only). Accordingly, Corning Inc. supplied various cordierite substrates with high porosity developed for GPF applications as well as substrates with medium porosity as shown in Table 3.4. KEX 200/8 with small medium pore diameter has been developed for uncatalyzed GPF use in add-on GPF systems.

Table 3.4 Specifications of selected GPF substrates supplied by Corning.

Selected sample	**% porosity**	**Medium pore diameter (d_{50}, µm)**
AC 200/12	50.56	20.74
KEX 200/8	57.22	11.67
KEM 300/8	64.60	20.38
HCW 200/12	65.76	20.93

Then, substrates supplied were wash-coated by TWC or others, serviced by Hyundai Motor Company. As indicated in Table 3.5, catalyst lodings were varied from 25 g/L to 50 g/L and 100 g/L, which are designated to be 1X, 2X and 4X, and PGM loading in washcoating was fixed to be 0.5g/ft^3. These TWC-coated filters were examined in the flow reactor to evaluate gaseous emissions as well as particulate emissions at different temperatures, exhaust flow rates and fuelcut operating conditions.

Table 3.5 Catalysts-coated GPF supplied by HMC.

Selected Samples	**Catalyst Coating**	**Loading (g/L)**	**PGM loading (g/ft^3)**
AC 200/12 KEM 300/8 HCW 200/12	w/ PGM, OSC, TWC w/ TWC w/ TWC	50 25, 50 and 100 50	0.5 0.5 0.5

In order to evaluate TWC/GPF performance, several evaluation factors were examined in this work. As ash was found to be positive in soot oxidation reactivity while it was known to deactivate TWC functions, impacts of ash loading on TWC/GPF were considered. Accordingly, particle mass & number emissions and gaseous emissions were measured in the downstream of TWC/GPF with ash loading. Since it is of great interest how pressure drop changes with soot loading at certain levels of ash loading, pressure drop was also measured. TWC and GPF performance is influenced by temperatures and exhaust gas flow rates, so gaseous and particulate emissions were evaluated at different temperatures and flow rates with varying engine operating conditions. Also, fuel-cut operating strategy was applied to understand regeneration process in consideration of actual engine operations. One example of the test protocol is described in Figure 3.31.

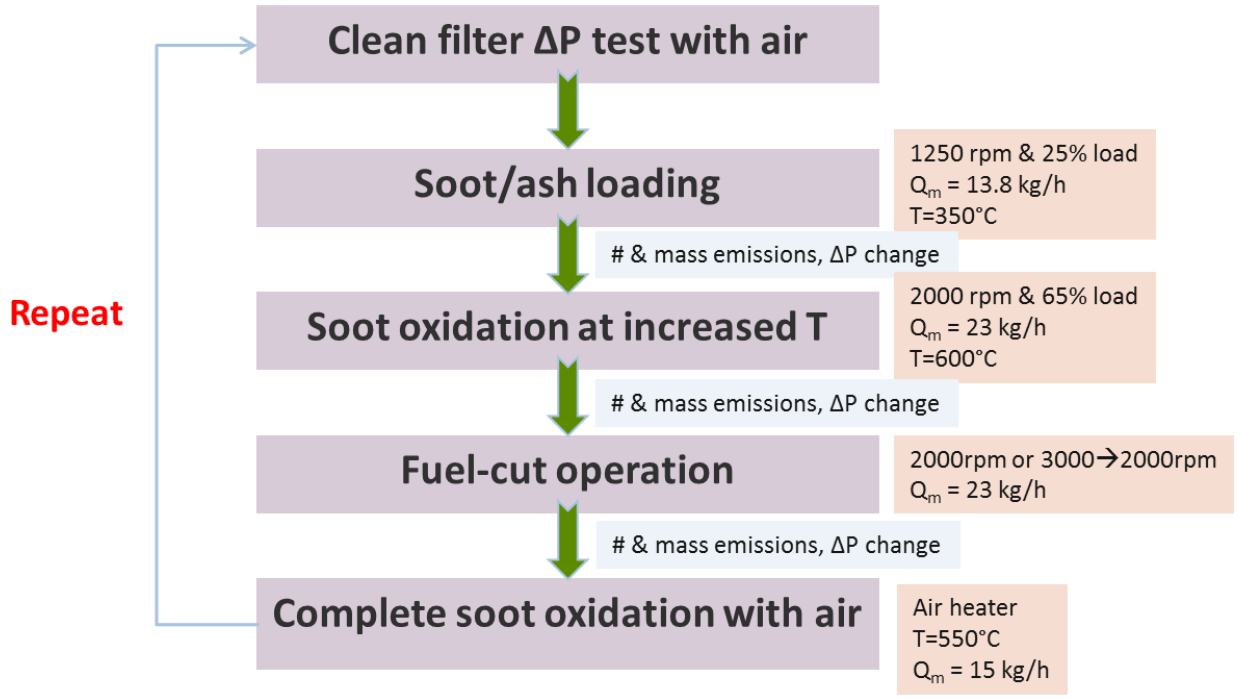

Figure 3.31 TWC/GPF test protocol for filtration and regeneration processes.

Catalyst coating effects on pore structure were investigated for different filter substrates by Corning Inc. by using mercury intrusion porosimeter. HP200/12 and HP300/8 are HCW 200/12 and KEM 300/8, respectively, in Table 3.4. The porosity of AC200/8 decreased from 50.56% to

47.92% with catalyst coating of 2X, while that of HP200/12 decreased slightly from 65.76% to 64.17% with the same amount of coating as shown in Figure 3.32. Likewise, HP300/8 with high porosity showed minor decreases in porosity with increased catalyst coating. Therefore, it appeared that catalyst coating results in minor decreases for both medium and high porosity filters. However, coating effects were shown to be more significant for medium pore diameter and pore size distribution. Medium pore diameter of AC200/8 decreased from 20.74 nm to 9.17 nm with catalyst coating of 2X. With the same amount of catalyst coating, however, medium pore diameters of HP200/12 and HP300/8 experienced a slight decrease from 20.93 nm to 18.67 nm and 20.38 nm to 18.82 nm, respectively. The wide shift in pore size distribution by catalyst coating was more obvious with the medium porosity filter than with the high porosity filters. Although changes in pore structure are minor with low and medium coatings for the high porosity filter, they could be huge with high coating even for high porosity filters as shown in the figure. Therefore, benefits of high porosity seem to be lost with catalyst coating of 100 g/L as indicated in the decrease in medium pore diameter and widening in pore size distribution.

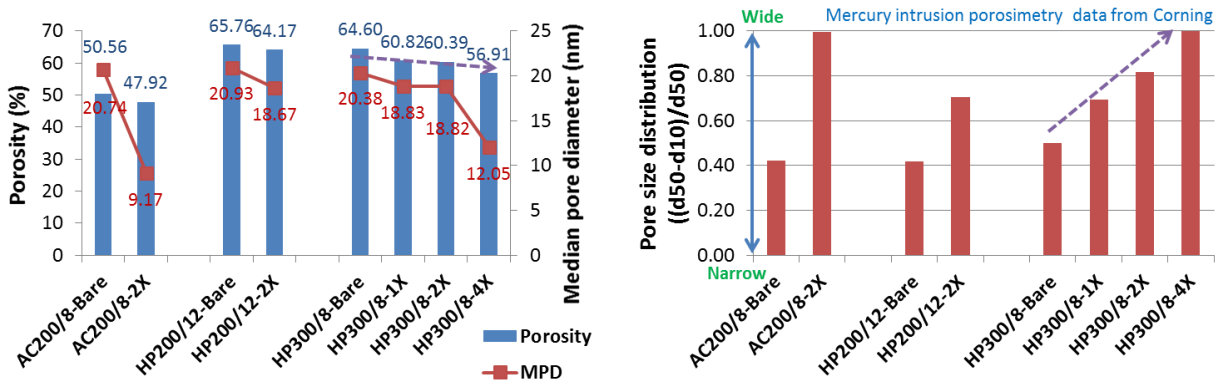

Figure 3.32 Pore structure analysis of bare and TWC-coated GPFs by mercury intrusion porosimetry.

Pressure drop increases were also examined with soot loading for uncatalyzed and catalyzed filters. Figure 3.33 shows pressure drop changes with soot loadings of 0.05 g/L, 0.10 g/L and 0.15 g/L. The pressure drop of clean filters increased significantly with catalyst coating of 2X for AC200/8 (100 to 240 kPa/(m^3/sec)). However, the increase was observed to be much mild with catalyst coating for HP300/8. Likewise, the increase in pressure drop with soot loading was more noticeable for AC200/8 than for HP300/8. Overall, the increase in pressure drop with soot loading was shown to be minor for catalyzed high porosity filters. These results indicate that catalyst coating and soot loading affected pressure drop in a mild way, when high porosity filters are used. This is because high porosity filters have a large capacity in pores to be loaded with soot and catalyst, compared to medium porosity filters.

Figure 3.34 explains the evolution of filtration efficiency with soot loading for various filter types. Uncatalyzed AC200/8 could reach the max point with soot loading of only 0.05 g/L despite relatively low initial filtration efficiency of 70%. Catalyzed high porosity filters, which showed relatively high initial filtration efficiencies, moved slowly toward the max filtration efficiencies, so they required soot loading of around 0.1 g/L to reach the max point. This result means that high initial filtration efficiency is achieved for high porosity filters with catalyst coating, but relatively high particle penetration would occur with high porosity filters, in comparison with the medium porosity filter. While there benefits low backpressure increase with soot loading, there would be a marginal penalty of particle penetration through filters when high porosity filters are used. As examined in the previous section, the Greenfield gap was investigated for high porosity filters in the beginning of the filtration as the level of catalyst coating was changed. As shown in Figure 3.34b, initial filtration efficiencies of 70% to 98% were achieved in the examined size range and their overall changes with catalyst coating were found to be marginal. The minimum filtration efficiencies occurred in the size range of 40nm to 60nm, so particles that penetrated the high porosity filters appeared to be relatively small in terms of mass concentration. The figure also indicates that with catalyst coating, the particles that penetrate the filter mostly tend to slightly decrease from 60 nm to 40 nm. Because catalyst coating decreased median pore diameter and widened pore size distribution as explained in Figure 3.32, modified pore structures of filters seemed to affect particles in the smaller range, resulting from the combination of diffusion and impact effects. Although the particle sizes of Greenfield gaps were observed to be larger than what we observed, they

tended to be smaller with soot loading according to other research because soot loading also modified pore structures in the same way of catalyst coating
[4].

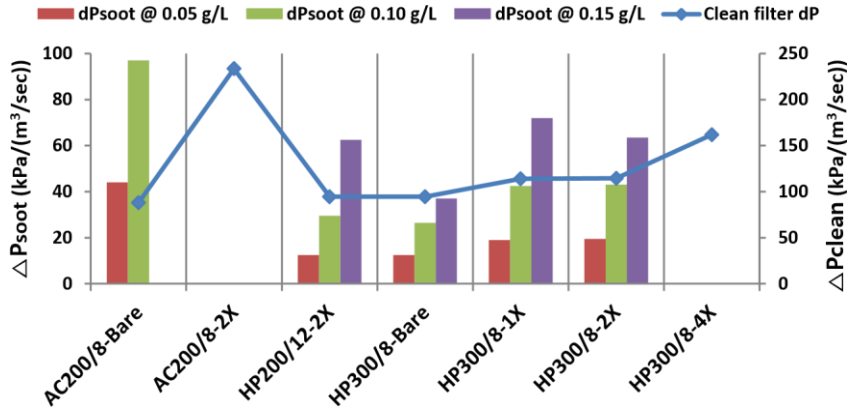

Figure 3.33 Pressure drop of clean filters without ash loading and pressure drop changes with soot loading.

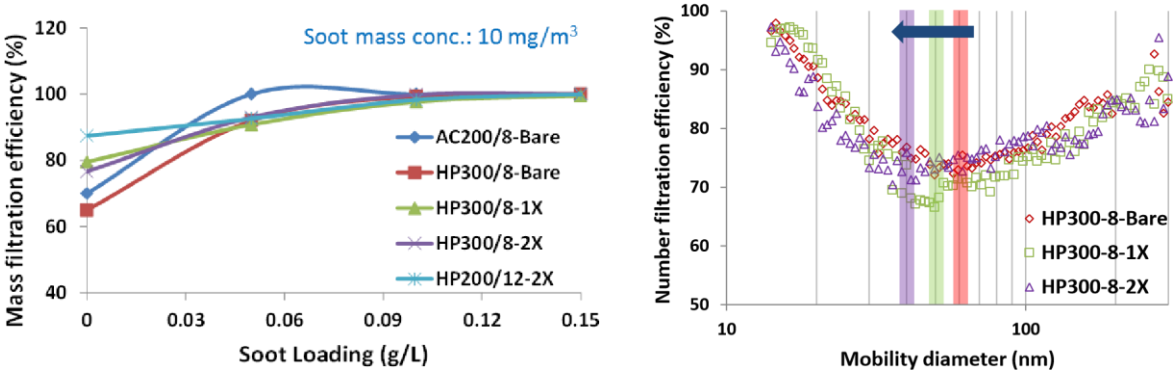

(a) (b)

Figure 3.34 (a) Evolution of mass filtration efficiency of high porosity filters with soot loading, and (b) initial number filtration efficiency of high porosity 300/8 filters at different sizes.

3.6 Evaluation of filtration and regeneration processes with ash loading

Impacts of ash loading on particle number and mass emissions were investigated as shown in Figure 3.35. HP200/12 with catalyst coating of 50 g/L was examined at 1250rpm-25% load, when soot mass concentration was kept at 10 mg/m^3. Pressure drop changes and particle penetration were compared for the fresh filter and filter with ash loading of 2 g/L. The fresh filter showed depth filtration regime in the soot loading range of 0 to 0.2 g/L and soot cake gradually increased from soot loading of 0.2 g/L. During the process, mass filtration efficiency reached the max point of almost 100% with soot loading of 0.12 g/L, beginning at the initial filtration efficiency of 87%. In comparison, the filter with ash loading had almost negligible depth filtration regime and pressure drop gradually increased with soot cake formation, in which the increasing slope in pressure drop is much lower than did the fresh filter. The short depth filtration regime and lower slope were anticipated from the previous work [5], because

filter pores are mostly plugged with porous ash from the start of the test. As a consequence, the initial filtration was already 98%. Figure 3.35b also indicates that particle penetration was very low with ash loading due to the same reason: the initial filtration of no ash filter was 81%, while that of ash loading of 2 g/L was 98%. These results explain that particle emissions and pressure drop are benefited with soot loading when it was not significant.

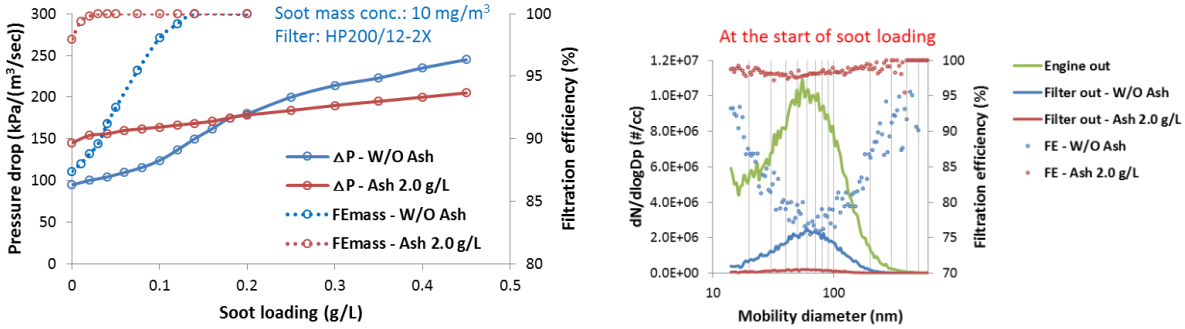

(a) (b)

Figure 3.35 Evaluation of HP200/12 filter with and without ash loading: (a) evolution of pressure drop and mass filtration efficiency, and (b) particle number distributions and number filtration efficiency.

Continuous regeneration was performed for the filters with no ash and ash loading, when soot loading reached 0.45 g/L. For the experiments, the engine was operated at 2000rpm-65% load to increase exhaust temperature, where soot mass concentration was 1.0 mg/m^3. The pre-GPF temperature was 550°C and post-GPF temperature was 650°C for the regeneration test. As shown in Figure 3.36a, the fresh filter shows that pressure drop gradually increased from 350 to 500 kPa/(m^3/sec). The relatively big increase in the pressure drop in the initial stage is because exhaust temperature was not saturated yet after the engine mode was switched from 1250rpm25% load. Therefore, it appears that soot cake formation and soot oxidation were balanced at 500 kPa/(m^3/sec) with this relatively low soot mass concentration, indicating that continuous regeneration occurred at this condition, although it was not the level to reduce pressure drop. In comparison, the filter with ash loading shows that pressure drop was lowered in the initial stage and then increased like the pattern shown in the no ash case. Since ash and soot may have been in close contact in the initial stage, soot oxidation seems to be enhanced for a certain period of time until soot in contact was all oxidized, as proposed from TGA experiments. This is the first evidence that ash accumulated in filter could actually help soot oxidation. After then, incoming soot resulted in increasing pressure drop in a mild way and becoming saturated at 440 kPa/(m^3/sec) as a similar pattern shown in the fresh filter. Heavy ash loading will eventually increase pressure drop, but light ash loading seems to help lower pressure drop because soot oxidation was enhanced. It should also be noted that inlet temperature of 550 °C and outlet temperature of 650 °C were not enough to lead to lowering pressure drop, because O_2 concentration was too low for soot oxidation. It was typically known that soot did not remain in GPF due to high exhaust temperatures in GDI engine, but it was obvious that the inlet O_2 concentration of almost 1% was mostly used for TWC function, leaving a negligible amount of O_2 at the exit of the filter.

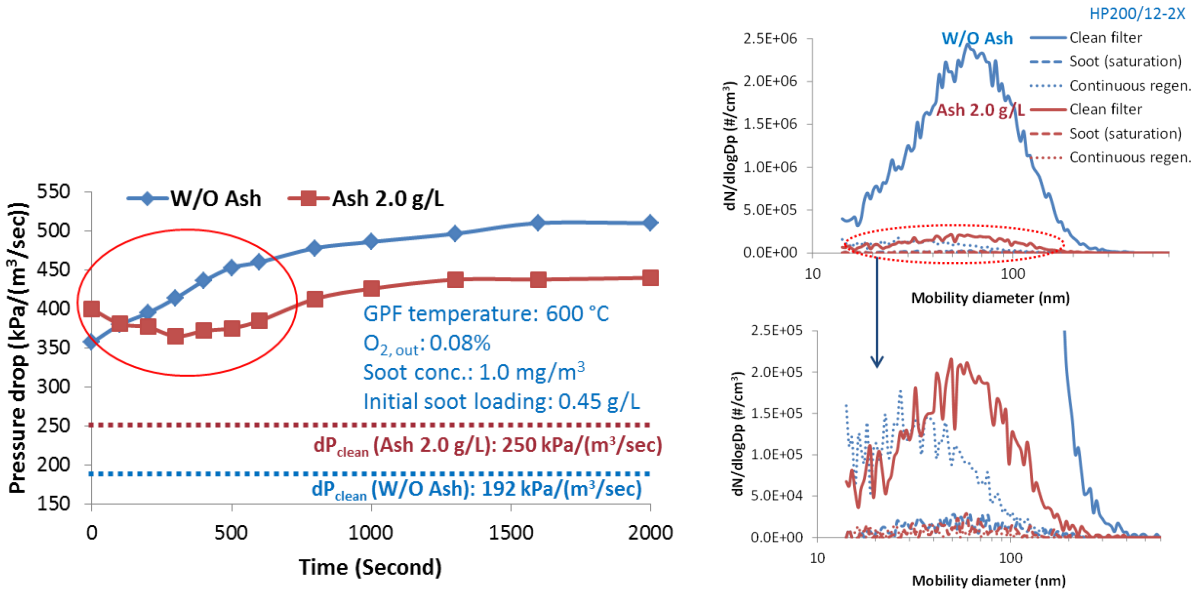

(a) (b)

Figure 3.36 Impacts of ash loading on filter performance: (a) Pressure drop changes with time during regeneration process, and (b) particle penetration by size distributions during saturated soot loading and continuous regeneration.

Particle penetration was also examined during continuous regeration modes. It is obvious that particulate emissions escaped from the filters were extremely low even with the fresh filter. It is interesting that with the fresh filter, particle penetration increased during continuous regeneration process, compared to that during the soot saturation mode, before switching to the continuous regeration mode. Because soot trapped in pores was oxidized continously, resulting in pore opeing, more particles could escape the filter durigh the regeneration process. In comparison, pores plugged with ash particles did not experience pore opening with soot oxidation, particle penetration was almost negligible for the filter with ash loading.

As soot oxidation seemed to be not active due to low O_2 concentration, fuel-cut operations were performed to understand soot oxidation process in GPF. For the experiments, while the engine was operated at 2000rpm-65% load, the throttle was immediately released to 1200 rpm, conducting fuel-cut for 10 seconds for each case and was resumed to the original operating condition. As shown in Figure 3.37, for the filter with no ash loading, three times of fuel-cut operations did not lead to a noticeable decrease in pressure drop. For simulating actual vehicle operation, the engine was stopped for a short period of time and resumed to the original operating condition at 2000 rpm. As shown in the figure, pressure drop dramatically dropped from 450 to 360 kPa/(m^3/sec) after the shut-down of the engine. When fuel-cut operations were subsequently applied, pressure drop decreased noticeably from 360 to 300 kPa/(m^3/sec). While soot mass emissions escaped from the filter were low before engine shut-down, they were relatively high after engine shut-down. The left figures in Figure 3.37 indicate that particle number emissions also appreciably increased during fuel-cut operations after engine shut-down. Since much amounts of soot particles trapped in the filter were oxidized at high exhaust temperatures with increased O_2 concentration during engine shut-down, fuel-cut operations could further oxidize soot remaining in the filter, resulting in increased particle penetration

with pore opening. Based on these results, particle penetration was sumarized in Figure 3.38. Therefore, it is assumed that the reason why soot accumulation in GPF is insignificant is that most soot is oxidized at hot exhaust temperatures with increased O_2 availability, resulting from various transient modes. In the same manner, the filter with ash loading of 2 g/L was evaluated in terms of pressure drop and particle penetration. Fuel-cut modes induced a gradual decrease in pressure drop from 450 to 400 kPa/(m^3/sec). Particle mass and number emissions escaped from the filter were observed to be very low, as evidenced in the right side of the figure (Please note that the unit of particle number is one order lower than those in the center and left figures). Although pressure drop decreased, pore opening would not occur because filter pores were tightly plugged with ash loading. Since the ash-loaded filter had a pattern of slow increase in pressure drop as observed in Figure 3.35, soot may have been mostly oxidized by fuel-cut operations probably because of enhanced soot oxidation by ash. Because this conclusion is hard to be made only with pressure drop data at engine operating modes, however, further examination is required by measuring CO and CO_2 emissions while performing laboratory tests using simulating gases.

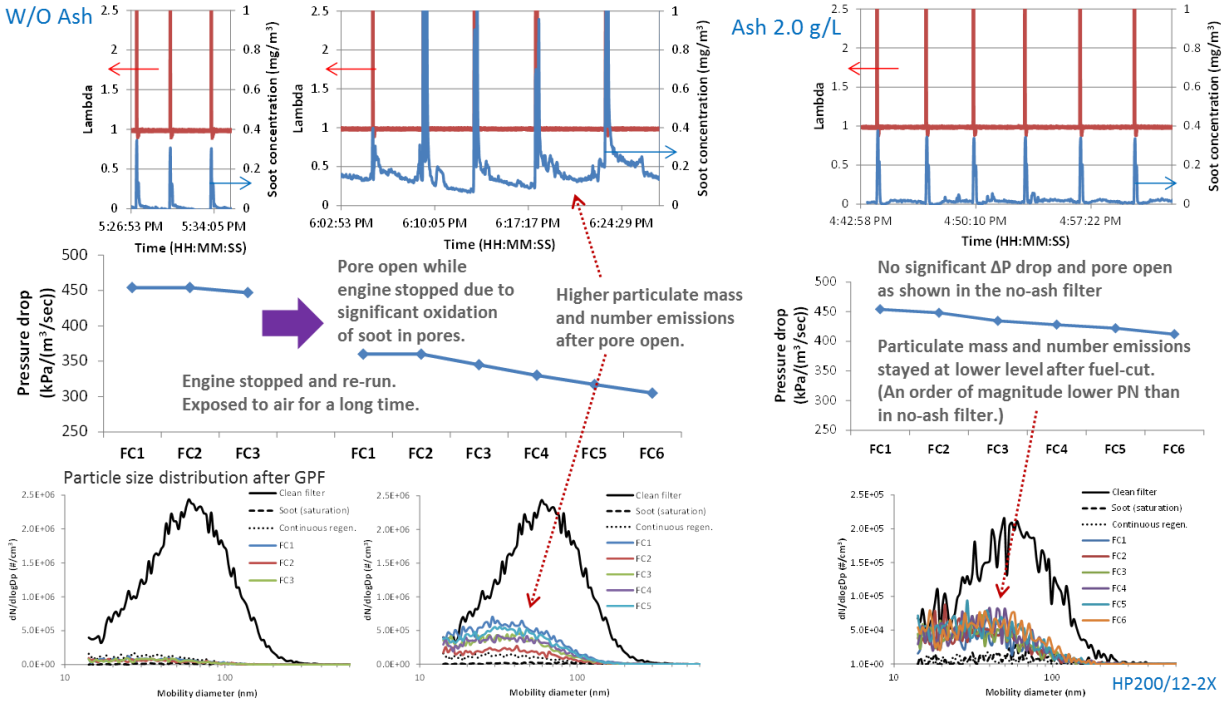

Figure 3.37 Impacts of fuel-cut operations on pressure drop and particle penetration.

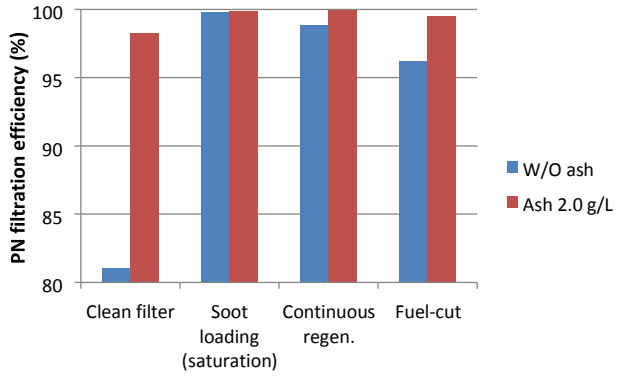

Figure 3.38 Summary of number filtration efficiency at various conditions for the filters with and without ash loading.

Figure 3.39 shows SEM analysis of ash loading in an aged GPF taken out of a vehicle that had run 100k miles. An ash layer was formed on top of the filter from a cross-section view. It is apparent that pores are fully plugged with ash particles, so the top side does not show any pores open. Even though GPF that had ash loading with acceleration test has not been examined for post-Mortem analysis, it is thought to have significant ash loading in pores, similar to aged filters. As evidenced with DPF case [6], ash layers tend to be denser with increased loading, resulting in decreased permeability, leading to increased pressure drop. If this trend is applied to GPF, it seems inevitable that TWC functions adversely because gaseous emissions would be kept from contacting catalysts with ash loading. Therefore, gaseous emissions were examined with ash loading in the following section to better understand its impacts on TWC functionality.

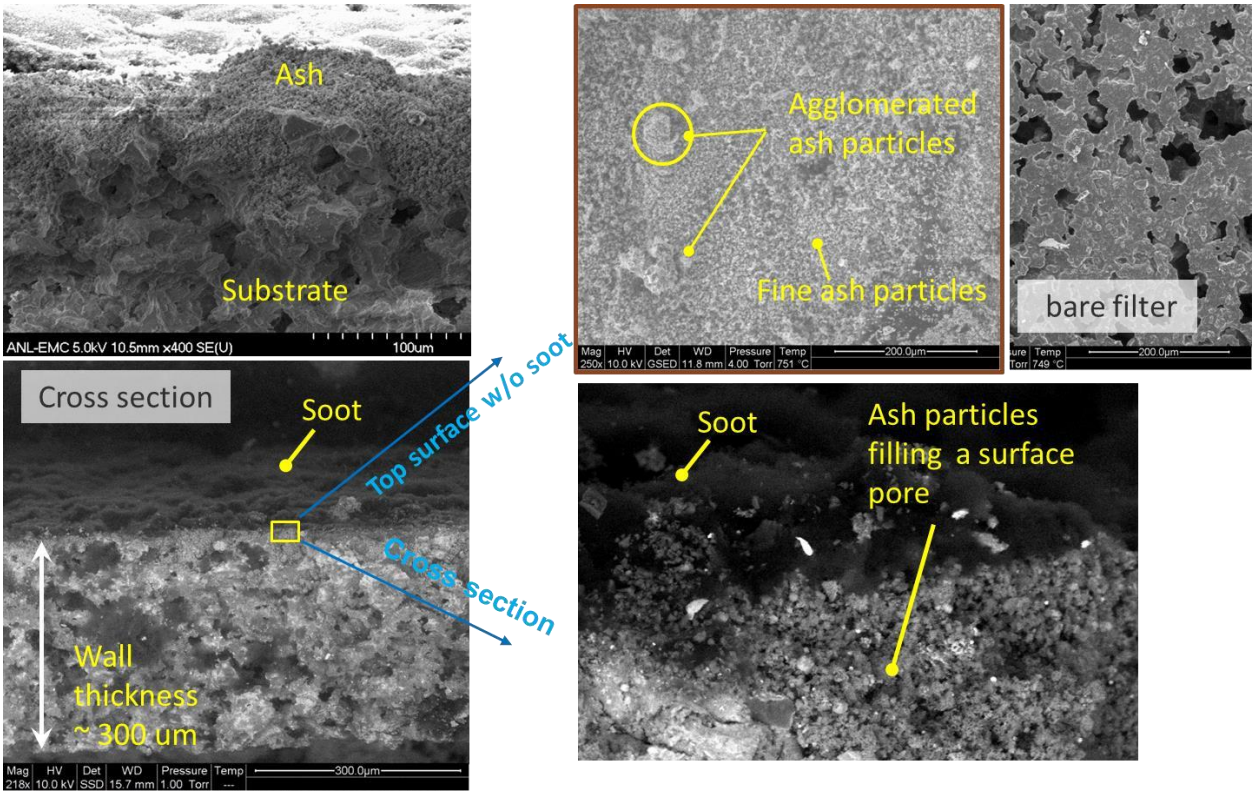

Figure 3.39 SEM analysis of a field-aged filter.

3.7 Evaluation of three-way catalyst performance with soot and ash loading

Effects of soot loading on TWC performance were examined for fresh HP300/8 with catalyst coating of 50 g/L. For soot loading, the engine was operated at 1250rpm-25% load with advanced fuel injection at 330° bTDC. As soot loading increased from 0 to 600 mg/L, conversions of NOx, THC and CO continuously decreased down to 35% (Figure 3.40a). While the inlet temperature was maintained at around 315 °C, the outlet temperature also decreased gradually, resulting from lower activation of catalysts. Therefore, it appears that catalytic performance can be lowered with soot loading at this relatively low temperature. When soot

was loaded in the filter as much as 600 mg/L, the inlet temperature was increased up to 370 °C as shown in Figure 3.40b, by increasing engine load with default injection timing. Gaseous emissions conversions were resumed in a short time, indicating that soot loaded in the previous procedure did not adversely impact gaseous emissions conversions at this temperature. Also, it was verified that the catalytic performance was immediately resumed to the initial level without soot loading, when the inlet temperature returned to 315 °C from 370 °C. Since much of soot in the filter still remained without oxidation at that relatively low temperature, soot loading seems not affect catalytic performance even at this low temperature with this operating procedure. Instead, the amount of incoming soot toward TWC/GPF seems to affect catalytic activation, but adsorption of gaseous emissions could increase at high soot emissions conditions, lowering catalytic performance when inlet temperatures are below 350 °C. However, it should be noted that since soot loading in GPF will be much lower at actual operating conditions than at this specific operating condition, adverse soot loading impacts may not be critical. Further investigation will continue.

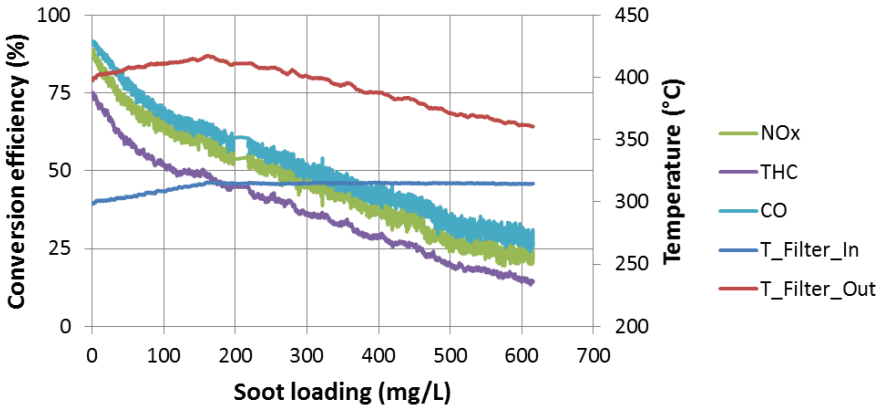

a)

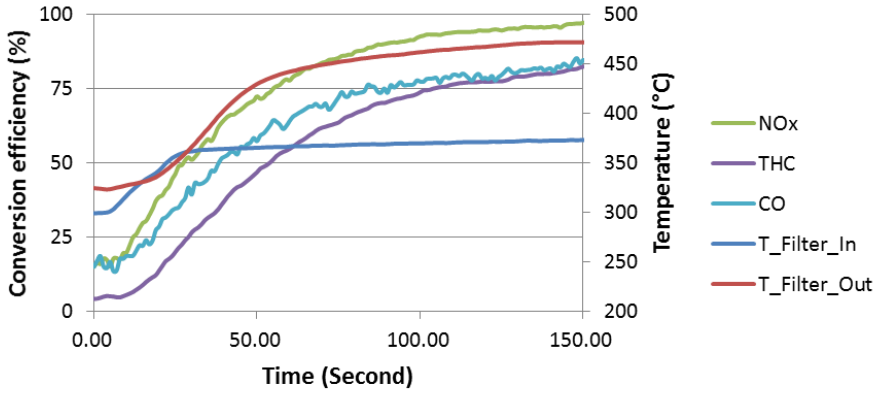

(b)

Figure 3.40 (a) Gaseous emissions conversions with soot loading at inlet temperature of 315 °C, when the high soot emissions condition was applied, and (b) gaseous emissions conversions with time at inlet temperature of 370 °C, when the low soot emissions condition was applied. Ash loading impacts on gaseous emissions conversions were examined in the inlet temperature range of 280 °C to 550 °C, as shown in Figure 3.41. These points were taken at

each temperature when soot loading was negligible. The fresh TWC/GPF showed that conversions of NOx, THC and CO were observed to be more than 88% in the extended temperature range. With ash loading, those conversions dramatically dropped at temperatures below 350 °C. When inlet temperatures were over 350 °C, gaseous emissions conversions of ash-loaded filters were almost the levels of the fresh filter although there observed a slightly-decreasing trend in conversions. Since the activation of the catalyst was lowered with ash loading, it is evident that the outlet temperature apparently decreased when the inlet temperature was below 350 °C, as indicated in the figure. However, it was noted that when the inlet temperatures returned to lower temperatures than 350 °C from over 350 °C, gaseous emissions conversions remained high for a certain period of time like the no ash case, as shown in Figure 3.42. Somehow, hysteresis in TWC performance was observed, when the filters experienced increased temperatures. Gaseous emissions conversions will be further examined to see if emissions trends will shift with additional ash loading.

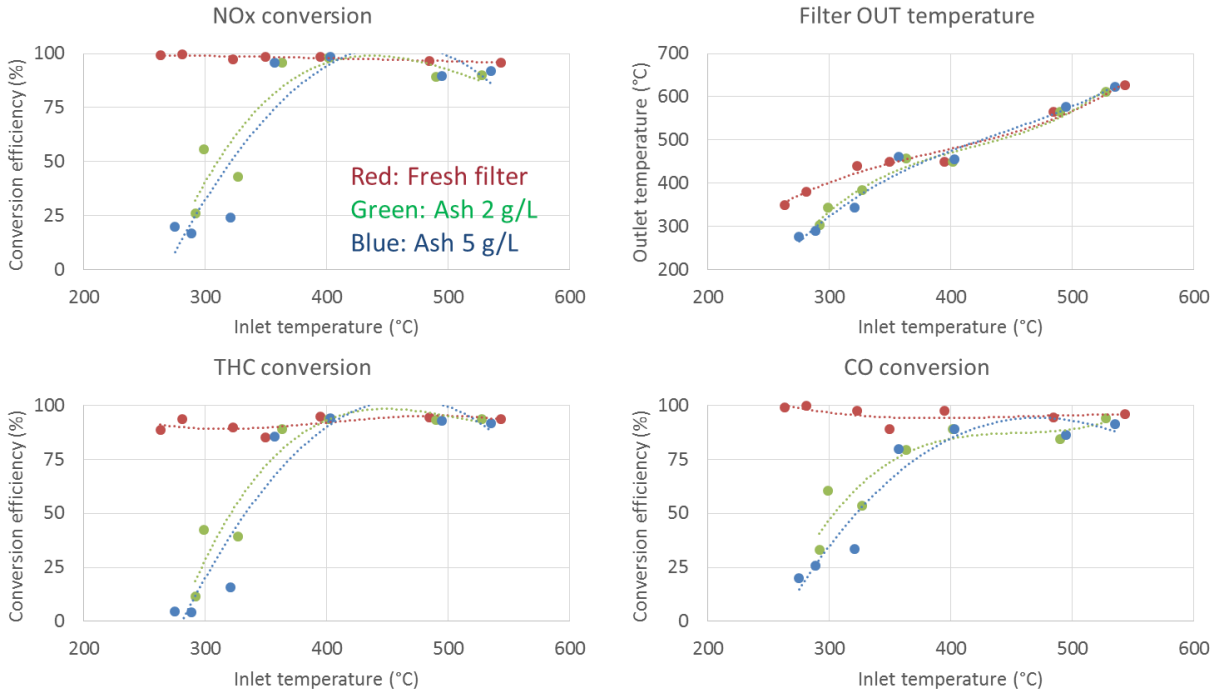

Figure 3.41 Gaseous emissions conversions as a function of inlet temperature with ash loading.

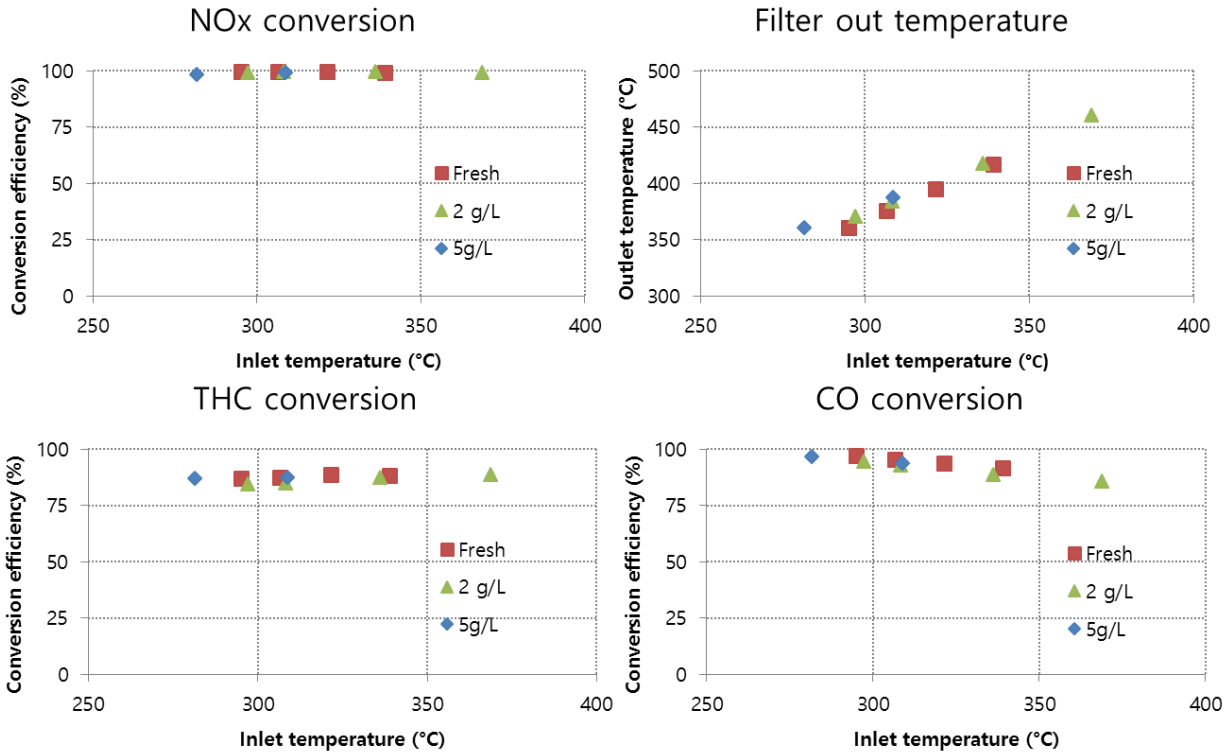

Figure 3.42 Gaseous emissions conversions as a function of inlet temperature with ash loading, when inlet temperatures returned from 530 °C.

4. Summary

-. 2.4L Hyundai production GDI engine was installed in an ANL dynamometer and a fullyinstrumented flow reactor was installed in the engine to examine filtration and regeneration processes in GPFs.

-. According to TEM analysis, GDI particulates were observed to be chain-like structures like particulates from other combustion sources. GDI particulates are in a broad size range from sub10-nm to several hundred nm and particles found in the sub-23-nm range appeared to be solid soot particles composed of amorphous and graphite-like soot particles.

-. When spark timing was fixed at constant, primary and aggregate particles tend to become larger with advancing fuel injection, which are in the comparable range of diesel particles. -. GDI soot samples appeared to be similarly ordered in carbon crystallites based on limited engine operating conditions.

-. According to TEM analysis, GDI soot taken at certain operating conditions experienced particle expansion when it was exposed to high energy beam, indicating that it contains high amounts of PAHs convertible into amorphous soot, distinct from diesel soot.

-. Cold transient modes produced around 50 time more soot mass emissions than do hot steady modes, based on the examined conditions, which is contributed from increased fuel-rich pockets and slow fuel vaporization, resulting from fuel wetting. Increased soot mass and number emissions are well correlated with inverse coolant temperature.

-. Soot emissions occurred during fuel-cut operations despite no combustion process, because soot accumulated in piston top, cylinders and exhaust pipe was blown by reverse blow-by or/and detachment.
-. Around 10% of soot particles were effectively removed in TWC by diffusion and impact. The effect was shown to be more appreciable at low space velocities.
-. Ash particles contributed from engine-oil additives and TWC coating materials enhanced soot oxidation. In a series of experiments, nano-sized $CaSO_4$ formed from engine combustion promotes soot oxidation, because $CaSO_4$ with high surface area oxidizes soot by Redox mechanism.
-. Several filters with different porosities and cell size/width supplied from Corning were TWCcoated with different catalyst coatings serviced by HMC. According to mercury intrusion porosimetry provided by Corning, high porosity filters had relatively low impacts on filter pore structures with catalyst coating. High porosity benefits appeared to be lost with high catalyst coating of 100 g/L in this work, although TWC performance and others need to be further examined for the long-term evaluation.
-. Filtration efficiency moves slowly toward max point with high porosity filters, indicating particle penetration through high porosity filters is more noticeable than through medium porosity filters.
-. Low ash loading benefits filtration efficiency, so particle penetration is extremely low. Ash loading also shows enhanced soot oxidation when it is in close contact with soot, based on pressure drop analysis during regeneration process.
-. Inlet temperature of 550 °C seems not enough for soot oxidation, possibly because of low O_2 availability. The reason soot remains low in GPF could be because soot is mostly oxidized when O_2 is abundant at high exhaust temperatures through fuel-cut and/or engine-shut down.
-. Ash particles completely plug filter pores according to SEM-EDS analysis of a field-aged filter.
-. When soot mass concentration was increased by manipulating fuel injection timing, gaseous emissions conversions were found to decrease when inlet temperatures were below 350 °C. TWC performance seems to be influenced by incoming soot mass, rather than soot loading in filters when inlet temperature is below 350 °C.
-. Gaseous emissions conversions tend to decrease with ash loading, when inlet temperatures were below 350 °C. When the temperature returned to lower temperatures from over 350 °C, however, gaseous emissions conversions tend to be resumed to almost fresh levels, indicating there exists performance hysteresis with thermal effects.

Published papers from the CRADA project Refereed
journal articles

1. Heeje Seong and Seungmok Choi, “Oxidation-derived maturing process of soot, depend ent on O_2-NO_2 mixtures and temperatures,” Carbon, 2015, 93, 1068-1076.
2. Seungmok Choi and Heeje Seong, “Oxidation characteristics of gasoline direct-injectio n (GDI) engine soot: Catalytic effects of ash and modified kinetic correlation,” Combus tion and Flame, 2015, 162, 2371-2389.
3. H. Seong, S. Choi and K. Lee, “Examination of nanoparticles from gasoline direct-injec tion (GDI) engines using transmission electron microscopy (TEM),” International Journ

al of Automotive Technology, 2014, 15, 175-181.

4. Heeje Seong, Kyeong Lee, and Seungmok Choi, "Effects of Engine Operating Parameters on Morphology of Particulates from a Gasoline Direct Injection (GDI) Engine," SAE paper, 2013, 2013-01-2574.
5. Kyeong Lee, Heeje Seong, Stephen Sakai, Mitchell Hageman, and David Rothamer, "Detailed Morphological Properties of Nanoparticles from Gasoline Direct Injection Engine Combustion of Ethanol Blends," SAE paper, 2013, 2013-24-0185.

Publications in conference proceedings

1. Heeje Seong and Seungmok Choi, "Soot oxidation behaviors influenced by different oxidizing environments: O_2 only and O_2-NO_2 mixtures," SAE World Congress & Exhibition, 21 – 23 April, Detroit, MI (USA), 2015.
2. Heeje Seong and Seungmok Choi, "Investigation of sub-23-nm particles by using HRTEM: Existence of solid soot," 2015 CRC World Emissions Workshop, Long Beach, 22 – 25 March, CA (USA), 2015 (poster).
3. Seungmok Choi and Heeje Seong, "Lube oil-derived ash impact on GDI engine particulate emissions and soot oxidation reactivity," SAE 2014 Light-Duty Emissions Control Symposium, 9 – 10 December, Troy, MI (USA), 2014.
4. Heeje Seong, Kyeong Lee and Seungmok Choi., "Oxidative reactivity of particulates from a gasoline direct injection (GDI) engine," FISITA 2014 World Automotive Congress, F2014-CET-106, 2 - 6 June, Maastricht, The Netherlands.
5. Heeje Seong, Kyeong Lee and Seungmok Choi, "Unique properties of gasoline direct injection (GDI) engine particulate matter (PM): morphology, nanostructures, and oxidative reactivity," Cross-Cut Lean Exhaust Emissions Reduction Simulations (CLEERS) workshop, Dearborn, MI (USA), 2014.
6. Seungmok Choi, Heeje Seong and Kyeong Lee, "Oxidation characteristics of soot from a gasoline direct-injection (GDI) engine," Cross-Cut Lean Exhaust Emissions Reduction Simulations (CLEERS) workshop, Dearborn, MI (USA), 2014.
7. Heeje Seong and Kyeong Lee, "Morphological and nanostructural examinations of particulates from gasoline direct injection (GDI) engines: effects of fuel, injection timing, engine load and air/fuel ratio," 2nd Joint Workshop of US-ASIA TransTech R&D Cluster, Argonne, IL (USA), 2013.
8. Seungmok Choi, "Study on particulate filters for gasoline direct injection Engine applications," 2nd Joint Workshop of US-ASIA TransTech R&D Cluster, Argonne, IL (USA), 2013.

References

1. Barone, T.L., Storey, J.M.E., Youngquist, A.D., and Szybist, J.P., "An Analysis of DirectInjection Spark-Ignition (DISI) Soot Morphology," *Atmospheric Environment*, 49, pp. 268274, 2012.
2. Yazicioglua, A. G., Megaridis, C. M., Campbell, A., Lee, K. –O., and Choi, M. Y., "Measurement of Fractal Properties of Soot Agglomerates in Laminar Coflow Diffusion Flames Using Thermophoretic Sampling in Conjunction with Transmission Electron Microscopy and Image Processing," *Combust. Sci. and Tech.*, Vol. 171, pp. 71-87, 2001.

3. Storey, J. M., Lewis, S., Szybist, J., Thomas, J., Barone, T., Eibl, M., Bafziger, E., and Kaul, B., "Novel Characterization of GDI Engine Exhaust for Gasoline and Mid-Level Gasoline-Alcohol Blends," SAE paper, 2014-01-1606, 2014.
4. Stewart, M., "Fuel-Neutral Studies of Particulate Matter Transport Emissions," Vehicle Technologies Office Merit Review 2014, Washington D.C., 2014.
5. Sappok, A. and Wong, V., "Ash Effects on Diesel particulate Filter Pressure Drop Sensitivity to Soot and Implications for Regeneration Frequency and DPF Control," SAE paper, 201001-0811, 2010.
6. Sappok, A., Kamp, C. and Wong, V., "Sensitivity Analysis of Ash Packing and Distribution in Diesel Particulate Filters to Transient Changes in Exhaust Conditions," SAE paper, 2012-011093, 2012.

Acknowledgement

This work was supported by the Advanced Combustion Engines Program at the US Department of Energy, Office of Vehicle Technologies under Contract No. C1200101. The authors appreciate support from Corning, Inc. and Hyundai Motor Company for the project. Furthermore, the use of the TEM and Raman microscope at the Center for Nanoscale Materials facility and the use of XANES and synchrotron XRPD at the Advanced Photon Source were supported by the U.S. Department of Energy, Office of Science, Office of Basic Energy Sciences.

Energy Systems Division
Argonne National Laboratory
9700 South Cass Avenue, Bldg. #362
Argonne, IL 60439

www.anl.gov